

Thin-Film-Engineered Self-Assembly of 3D Coaxial Microfluidics with a Tunable Polyimide Membrane for Bioelectronic Power

Aleksandr I. Egunov^{1*}, Hongmei Tang¹, Pablo E. Saenz¹, Dmitriy D. Karnaushenko¹, Yumin Luo^{1,2}, Chao Zhong³, Xinyu Wang³, Yang Huang⁴, Pavel Fedorov¹, Minshen Zhu^{1*}, Daniil Karnaushenko^{1*} and Oliver, G. Schmidt^{1,5,6*}

¹ Research Center for Materials, Architectures and Integration of Nanomembranes, Chemnitz University of Technology, Chemnitz, Germany.

² Chair of Microsystems Technology, Ruhr University Bochum, Bochum, Germany

³ Shenzhen Key Laboratory of Materials Synthetic Biology, Key Laboratory of Quantitative Synthetic Biology, Shenzhen Institute of Synthetic Biology, Shenzhen Institutes of Advanced Technology, Chinese Academy of Sciences, Shenzhen, China.

⁴ Department of Physics and Materials Science, City University of Hong Kong, Hong Kong, China.

⁵ Material Systems for Nanoelectronics, Chemnitz University of Technology, Chemnitz, Germany

⁶ Nanophysics, Dresden University of Technology, Dresden, Germany

*Corresponding authors

E-mail: aleksandr.egunov@main.tu-chemnitz.de,

E-mail: minshen.zhu@main.tu-chemnitz.de,

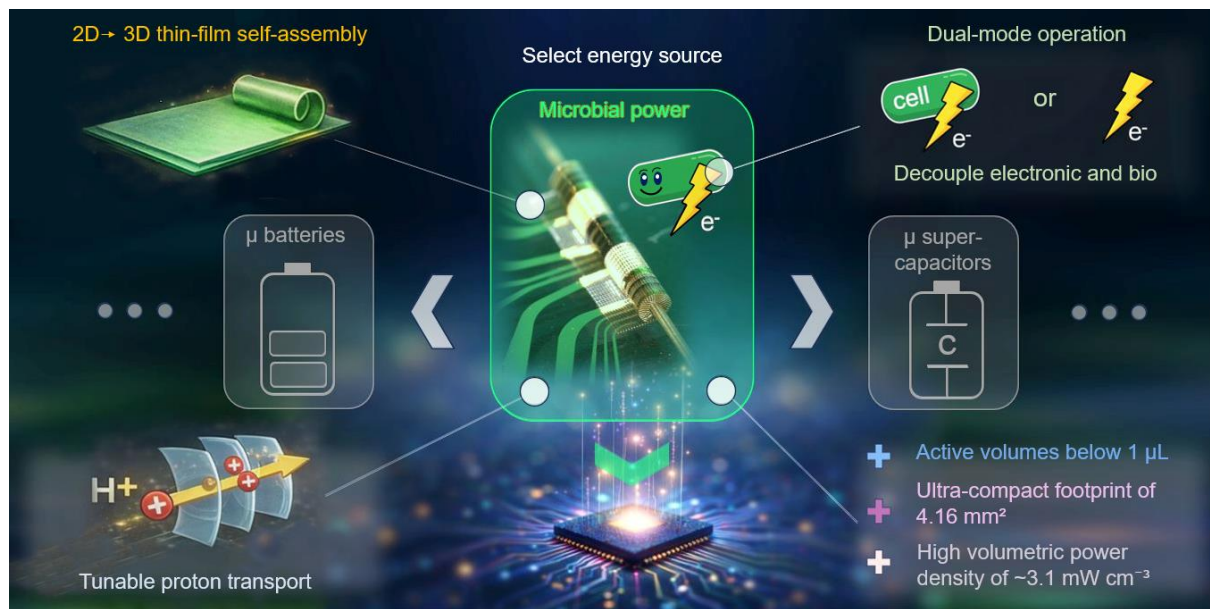
E-mail: daniil.karnaushenko@main.tu-chemnitz.de,

E-mail: oliver.schmidt@main.tu-chemnitz.de.

Highlights

- A bottom-up, strain-induced self-assembly strategy transforms 2D thin-film stacks into 3D coaxial Swiss-roll microsystems.
- Monolithic integration of a lithographically patterned, chemically tunable polyimide nanomembrane serves as a programmable proton-exchange component.
- Ultra-compact bioelectronic power supply achieves a volumetric power density of ~ 3.1 mW cm $^{-3}$ within a 0.80 μ L active volume and a 4.16 mm 2 footprint.
- Sustainable dual-mode operation decouples microbial metabolism from power generation, eliminating biofouling and enhancing long-term stability.
- The platform demonstrates scalable fabrication (>85% yield) and provides a versatile architecture for integrable bio-hybrid devices.

TOC



Abstract

Thin-film self-assembly of three-dimensional (3D) microsystems presents a compelling route to integrate complex functionalities into ultracompact volumes, yet strategies for incorporating tunable ion-conducting elements remain limited. Here, we introduce a strain-induced self-assembly platform that transforms lithographically patterned multilayer thin films into functional 3D coaxial Swiss-roll microtubes with total active volumes below 1 μ L. A key innovation is the monolithic integration of a chemically tunable polyimide proton-exchange

membrane, enabling post-fabrication optimization of ionic transport. We further implement a dual-mode operational scheme that decouples microbial metabolism from electrochemical power generation, effectively eliminating biofouling and enhancing operational stability. This integrated bio-electronic microsystem achieves a volumetric power density of ~ 3.1 mW cm $^{-3}$ within an ultra-compact footprint of 4.16 mm 2 . Our work establishes a scalable thin-film engineering approach to create tunable, 3D-bioelectronic power sources for autonomous microsystems.

Keywords: Self-assembly, 3D microfluidics, Thin-film membranes, Coaxial structure, Microbial fuel cells, Bioelectronics

1 Introduction

The development of autonomous microsystems and bioelectronic interfaces is fundamentally constrained by the lack of scalable, integrable ultra-small microsystems [1] and sensors [2,3]. To address this, next-generation microbial fuel cells (MFCs) must not only miniaturize but also adopt manufacturing processes compatible with microelectronics [4,5]. MFCs generate electrical power through microbial oxidation of organic substrates under mild conditions, offering sustainable energy conversion from inexpensive, renewable fuels [6].

Conventional devices that rely on direct electron transfer [7] between microorganisms and electrodes face critical limitations. Microbial biomass occupies a significant portion of the electrode volume, promoting the formation of inactive biofilm layers that increase internal resistance over time. In contrast, electron transfer mediated by soluble redox mediators eliminates the need for direct microbe–electrode contact while maintaining efficient redox cycling [8]. This strategy enables a new class of systems, termed indirect flow-type MFCs (IFT-MFCs), demonstrated here for the first time.

The IFT-MFC concept decouples microbial metabolism from electrochemical power generation. During operation, microorganisms such as *Saccharomyces cerevisiae* reduce soluble mediators via bio-oxidation in an external bioreactor. The reduced mediators are then delivered to the anode chamber, where they transfer electrons to the electrode surface. On the cathodic side, an oxidized catholyte (e.g., ferri/ferrocyanide) is regenerated by atmospheric oxygen and recirculated. This modular design enables dual-mode operation: a cell-based mode

(Mode 1) for continuous mediator regeneration and a cell-free mode (Mode 2) for abiotic power generation, enhancing robustness and control.

At the microscale, microfluidic architectures provide a natural platform for implementing this concept [9], offering precise management of fluids and reactants [10] and improved kinetics [11]. The proton exchange membrane (PEM) plays a crucial role by facilitating ionic transport while preventing electrolyte mixing. Although hydrodynamic systems relying on laminar flow without a membrane have been explored, they require millimeter-scale electrode separations that increase internal resistance and offset the benefits of miniaturization [12]. Maintaining strict flow separation is essential, as even minor crossover can disrupt anaerobic conditions and cause electrochemical short-circuiting [13]. While laminar-flow systems [14] reduce mixing, membrane-based architectures [15] remain the most reliable for preventing self-discharge and ensuring long-term stability [16]. However, widely used ion-exchange materials such as NafionTM remain costly and difficult to integrate at microscale [17], motivating the exploration of alternative polymers [17,18].

At the microscale, conventional PEMs (NafionTM, cellulose acetate, polyvinylidene fluoride (PVDF)) pose additional challenges, including high interfacial resistance and poor compatibility with wafer-scale microfabrication[19–22]. To address these issues, polyimide (PI) has emerged as a mechanically robust, biocompatible, and microfabrication-compatible alternative [23]. PI is widely employed in microelectronics and enables ultrathin, scalable devices [24–27], as demonstrated in neural implants [28], implantable antenna [29] and sensors for biological applications [30,31]. Its flexibility also allows for 3D integration, increasing active surface area while maintaining a compact footprint.

Recent progress in self-rolled polymeric nanomembranes [29,32,33] and rolled-up microfluidics [34] has opened a new route toward highly integrated 3D energy systems. This strain-driven self-assembly approach represents a powerful bottom-up strategy for microsystems fabrication, where 2D nano- and micro-scale thin films are engineered to autonomously form complex 3D architectures. It combines miniaturization with structural and functional integration. When released, thin polymeric nanomembranes spontaneously form tubular microfluidic structures [35,36] that can be seamlessly integrated with on-chip electronic components such as impedance sensors [31] and thin-film transistors [28,37]. This coaxial geometry enhances ion transport and boosts energy density, as shown by recent demonstrations of tubular capacitors [38,39], supercapacitors [40], and batteries [41,42] highlight the versatility of such architectures for powering microscale systems.

In this work, we present a 3D Swiss-roll indirect flow-type micro–microbial fuel cell (IFT- μ MFC) (Fig. 1). A lithographically patterned PI [43] film incorporating planar electrodes is transformed into a coaxial 3D architecture through a strain-driven self-rolling [44]. This self-assembly provides concentric microfluidic channels separated by PI walls that function as the PEM.

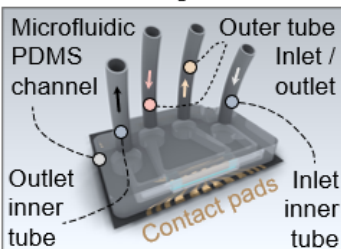
The resulting coaxial IFT- μ MFC (Fig. 1a) consists of an inner catholyte channel and an outer multi-winding anolyte channel. Both channels interface with an external microfluidic distribution network, enabling independent supply and control of the anolyte and catholyte. In operation, the anolyte and catholyte are housed in external reservoirs, while the on-chip rolled structure functions as the electrochemical converter.

This modular architecture (Fig. 1b) provides exceptional flexibility: By adjusting the external fuel containers, the system can be scaled or reconfigured to match varying energy requirements of microsystems. The combination of 3D self-assembly and microfluidic modularity [45] allows independent optimization of microbial culture, mediator regeneration, and electrochemical conversion, thereby enhancing both energy generation and operational stability.

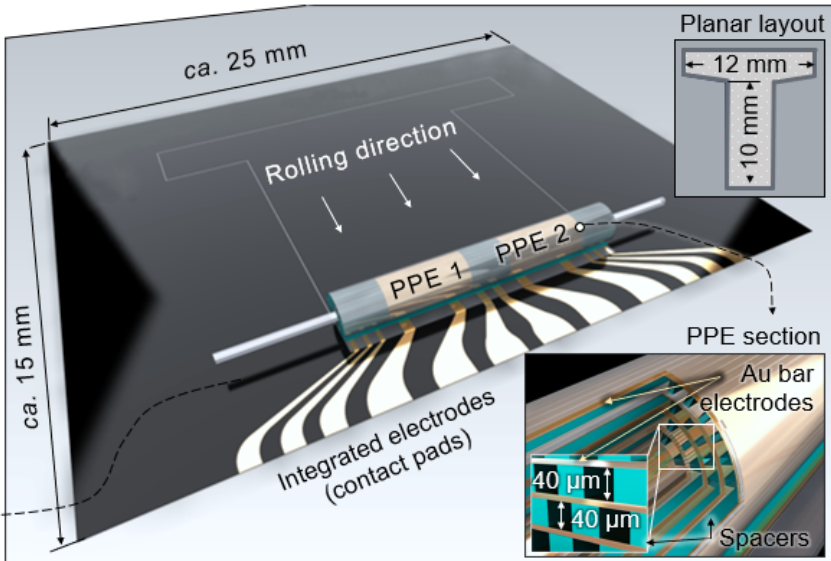
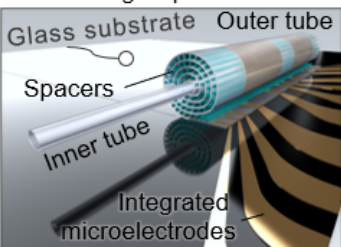
Overall, the Swiss-roll IFT- μ MFC establishes a versatile bio-electronic platform that combines biological and synthetic energy systems within a single, self-assembled structure, supporting dual-mode functionality for scalable integration into autonomous microsystems.

A Self-assembled coaxial Swiss-roll μ MFC with two PPEs sections

Microfluidic integration



Interwinding / Spacers



B Operating principles of coaxial Swiss-roll IFT- μ MFC in dual mode

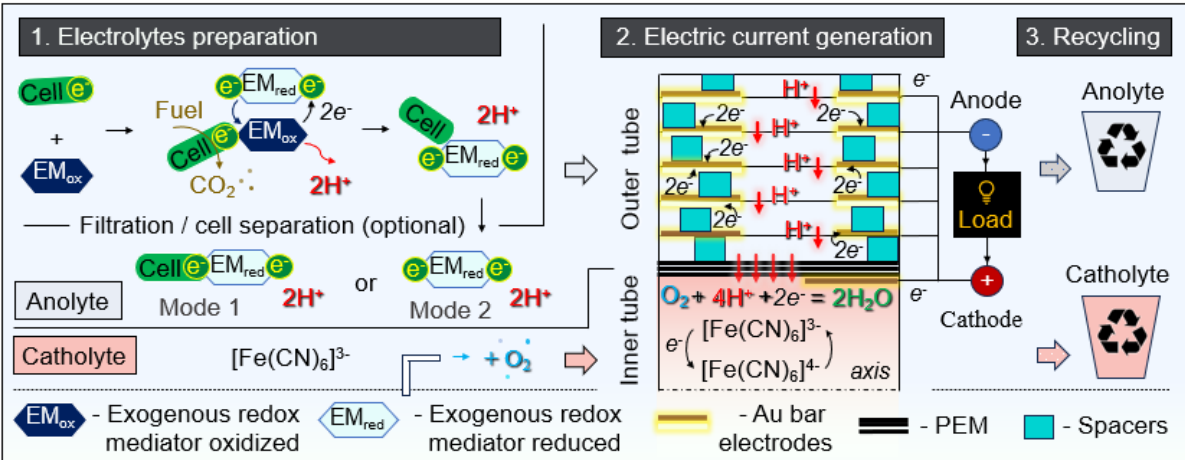


Fig. 1 Concept of the self-assembled coaxial Swiss-roll bio-electronic platform. **a** Schematic of the 3D self-assembled architecture integrated into a microfluidic system, showing the inner catholyte channel (inner tube) and the outer anolyte channel (outer tube) with integrated parallel-plate electrodes (PPEs). **b** Dual-mode operational scheme providing functional versatility. The platform supports two distinct states: a microbial mode 1 (functioning as a pure microbial fuel cell with integrated biology) and a cell-free mode 2 (operating as an abiotic electrochemical generator using pre-charged mediator). This allows the system to dynamically alternate between regenerative bio-power and stable electrochemistry, providing a robust interface between biological and electronic subsystems.

2 Experimental section

2.1 Design and fabrication of self-assembled coaxial Swiss-roll microtubes

The devices were fabricated using standard thin-film techniques, building on strained-layer rolling principles. Briefly, a ~500 nm sacrificial layer (SL) was deposited and patterned on a glass substrate, followed by a ~950 nm hydrogel (HG) swelling layer. A bottom electrode (BE, 10 nm Cr / 90 nm Au) was sputtered onto the HG. A ~500 nm polyimide (PI) layer was then spin-coated and patterned, followed by deposition of a second Cr/Au top electrode (TE). A reinforcing layer with a total thickness of ~1.3 μ m was built up in the first winding region by the successive deposition and patterning of two (or three) thinner polyimide layers to ensure mechanical stability without compromising flexibility. SU-8 spacers of varying thicknesses were lithographically defined to control interwinding spacing and act as fluidic channels. Anchors were formed by patterning windows in the SL to prevent lateral rolling.

The self-rolling process was initiated by selective dissolution of the SL combined with HG swelling, forming an inner tube with interdigitated electrodes (IDEs) and an outer tube with parallel plate electrodes (PPEs). To remove fabrication residues, the structures were treated with oxygen plasma (400 W, 20 min) through a ~1.4 μ m AZ5214 photoresist mask. Rolling was performed in diethylenetriaminepentaacetic acid (DTPA, pH 8, Sigma-Aldrich, \geq 98%), reproducibly yielding ~12 mm long coaxial tubes with diameters tunable from ~250 μ m to >500 μ m. Fabrication yield exceeded 85%.

Camphor-assisted drying: To preserve structure for microfluidic integration, coaxial rolls were immersed in a saturated camphor (\geq 98%, Alfa Aesar) solution in acetone. Upon withdrawal, a thin camphor layer crystallized as acetone evaporated. Complete sublimation under ambient conditions (4–5 h) left no residue and maintained winding uniformity.

Characterization: All deposition steps were monitored by stylus profilometry (Dektak, Bruker). Film quality and final structures were inspected by optical microscopy (Axioscope A1 and Keyence VHX, Zeiss). Scanning electron microscopy (SEM) was performed using a TESCAN GAIA3 microscope.

2.2 Microfluidic integration of coaxial system

Polydimethylsiloxane (PDMS) devices were fabricated by standard soft lithography using silicon wafer molds. PDMS (Sylgard 184, Dow, 10:1 base:curing agent) was cast, cured at 60 °C for 8 h, baked at 100 °C for 1 h, then demolded and port-punched.

Selective sealing: Uncured PDMS prepolymer was injected through six auxiliary lateral channels. The device was immediately placed on a 130 °C hotplate for 30 s to rapidly cure the PDMS and halt capillary-driven flow.

Fluidic connection: Devices were connected to a syringe pump (Pump 11 Pico Plus Elite, Harvard Apparatus) via PTFE tubing (OD 1/32, ID 0.30 mm; Darwin Microfluidics).

The integrity and isolation of the fluidic channels were characterized by flowing colored solutions. The inner and outer channels were perfused with aqueous solutions of an orange-fluorescent dye (Rhodamine B, $\geq 95\%$, Sigma-Aldrich), and a green-fluorescent dye (Fluorescein sodium salt, Sigma-Aldrich), respectively. For interconnection tests, a red food colorant was used. In open-configuration filling experiments, deionized water and, for enhanced visualization, a commercial food colorant were used.

2.3 Electrical integrity and geometry-dependent electrode characterization

Electrodes (3D IDE, PPE, and IDE–PPE sets) were characterized in a four-probe configuration to minimize cable parasitics. EIS was performed using a high-precision LCR meter (LCR-8105G, GW Instek) over 20 Hz – 5 MHz with a 500 mV AC excitation signal. Electrolytes included KCl ($\geq 99.5\%$, ITW Reagents, 10⁻⁴–1 M in 8 MΩ×cm DI water) and ethanol–water mixtures (using C₂H₅OH, $\geq 90\%$, AnalytiChem, diluted with DI water). Samples were equilibrated at 22–24 °C for 30 min prior to testing. Impedance data were analyzed to extract real/imaginary components and apparent capacitance.

2.4 Tuning proton exchange in a multi-winding membrane architecture

Lithographically fabricated PI PEMs, with a final thickness of ~ 1.3 μm , were mounted in PDMS frames. Proton transfer was evaluated in a macro-scale setup with two 3D-printed acrylic chambers (6 mL each), by adding 1 mL of 1 M HCl to 5 mL of 1 M KCl in the anodic chamber and monitoring the cathodic chamber pH over time. Membrane thickness was varied from 1 to 4 layers.

For resistance tuning, membranes were immersed in aqueous NaOH (1M, Sigma-Aldrich, $\geq 98\%$) at 22 °C for 1–60 min, achieving resistances from ~ 9 k Ω (1–2 min) to $\sim 250\Omega$ (~ 30 min). Prolonged immersion (> 1 h) reduced resistance below 100 Ω but induced fragilization.

PEM resistance (R_{mem}) extraction: R_{mem} was determined from EIS in symmetric two-electrode cells using parallel Au electrodes (area 1300 mm² each) in 1 M KCl. Resistance was extracted as the real component at 10³ Hz. Control experiments used NafionTM 117 (DuPont, 183 μ m) and KaptonTM (DuPont, 125 μ m). Each condition was tested in triplicate.

FT-IR characterization: FT-IR spectra were acquired using a Nicolet iS50 spectrometer (Thermo Scientific), averaging 128 scans at 4 cm⁻¹ resolution under nitrogen purge.

2.5 Component-level optimization of a bio-electrochemical energy system

Saccharomyces cerevisiae (baker's yeast, BY4741) was cultured anaerobically in YPD medium with 2% glucose (alpha-D(+)-Glucose, \geq 99%, Thermo Scientific) and introduced into the anodic chamber under anaerobic conditions.

Methylene blue (\geq 98%, Thermo Scientific) was used as the anodic exogenous mediator (EM) at concentrations from 1.25×10^{-6} M to 0.1 M in PBS (Pan Biotech, pH 7.4). The catholyte consisted of potassium ferricyanide (\geq 99%, Sigma-Aldrich) dissolved in a 1:1 mixture of 1 M KCl and glacial acetic acid.

Macro-scale MFCs were fitted with Au electrodes (10 nm Cr / 100 nm Au, 50–600 mm²) or graphite rods (99.95%, Sigma-Aldrich, 32–475 mm²). Polarization and power density curves were obtained by linear sweep voltammetry (LSV, 1 mV s⁻¹, Autolab PGSTAT101) from open-circuit voltage (OCV) to 0 V.

2.6 Sustainable dual-mode operation and performance benchmarking of a coaxial Swiss-roll bio-electronic platform

For cell-free operation, the anolyte was anaerobically filtered through 0.22 μ m PVDF membranes (Millipore) to remove yeast cells, yielding a purified solution of reduced mediator (EMred).

Coaxial μ MFCs employed PI membranes treated in NaOH (1 M, 30–180 min, 50 °C), achieving resistances from \sim 100 Ω to >1 M Ω . Polarization and power curves were recorded as described above.

3 Results and discussion

3.1 Design and fabrication of self-assembled coaxial Swiss-roll microtubes

We fabricated a polymeric nanomembrane stack using a strain-engineered self-rolling approach, building on previously reported methods [28,29]. This bottom-up self-assembly strategy transforms a lithographically patterned 2D thin-film stack into a functional 3D microsystem. The multilayer design integrated a sacrificial layer (SL), polyimide (PI), a hydrogel (HG) layer, thin-film gold electrodes, and SU-8 spacers, enabling controlled self-assembly and the direct integration of electrodes within the membrane stack (see details in Experimental section, Supplementary Figs. S1, S2). Upon selective dissolution of the sacrificial layer, a combination of built-in stress gradients and hydrogel swelling reshaped the planar stack into coaxial Swiss-roll tubes with precisely defined winding geometries. The design of the two-dimensional precursor was optimized to ensure stable rolling: a T-shaped layout proved optimal for the sequential formation of a stable coaxial configuration comprising an inner long tube and an outer short tube (Fig. 2, Supplementary Figs. S2, S3).

Optical microscopy confirmed the reproducible formation of \sim 12 mm-long coaxial structures with tightly aligned windings. The SU-8 spacer bars defined interwinding gaps from \sim 5 μ m to 50 μ m (Supplementary Fig. S4), providing direct control over the final tube diameter, which ranged from below 250 μ m to above 500 μ m. Scanning electron microscopy revealed mechanically robust rolling with no delamination or interfacial defects, confirming the structural integrity of the self-assembled architecture (Supplementary Fig. S4). The transition between the inner and outer tubes was stabilized by a \sim 1.3 μ m PI reinforcing layer in the first winding region, which prevented delamination and ensured a smooth curvature. Furthermore, lithographically defined anchors, directly coupled to the glass substrate, prevented uncontrolled lateral rolling and secured consistent coaxial assembly across the wafer.

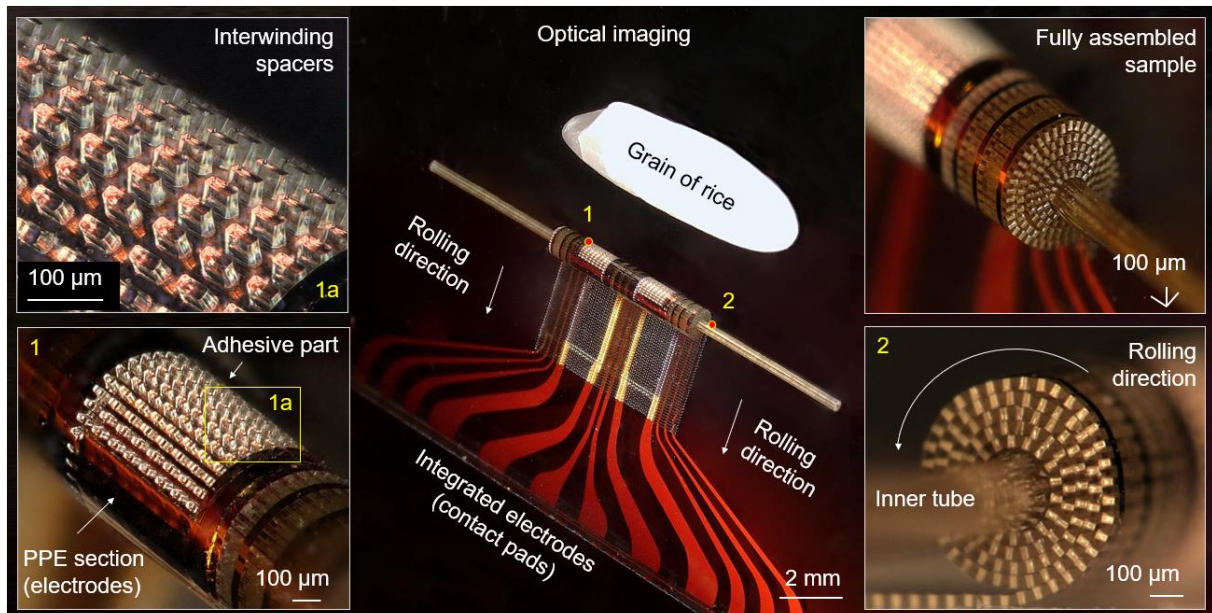


Fig. 2 Structural characterization of the self-assembled coaxial Swiss-roll microtubes. Optical microscope images of the fabricated 3D architecture after release from the substrate. The main panel shows an overview of the structure, highlighting the simultaneous formation of the inner and outer tubes. The **left** panel provides a magnified view of the SU-8 spacer bars that define the interwinding gaps and fluidic channels. The **right** panel shows a higher-magnification side view of the tube entrance, revealing the tightly packed and uniform windings that ensure mechanical stability.

The fabricated devices exhibited a yield exceeding 85% for mechanically intact coaxial structures per wafer, with minimal dimensional variability. These results demonstrate that the self-rolled fabrication strategy, a prime example of bottom-up microsystems engineering, enables the reproducible integration of electrodes, PI membranes, and spacers into mechanically robust 3D architectures. By tuning spacer dimensions and reinforcement layers, the tube diameter and interwinding geometry can be precisely engineered, establishing a structurally versatile and scalable platform for bio-electronic microsystems.

3.2 Microfluidic integration of coaxial system

The self-assembled coaxial structures were integrated into a polydimethylsiloxane (PDMS) microfluidic platform, enabling independent and stable fluidic operation of both the inner and outer channels (Fig. 3a). Prior to integration, the rolled structures were carefully dried using an established protocol [36] that exploits camphor sublimation to gradually replace residual water, thereby minimizing capillary forces and structural stress while preserving the intact coaxial geometry (see Experimental section and Supplementary Information).

Precise alignment of the coaxial tubes within the PDMS mould under optical microscopy ensured correct port registration. Liquid PDMS, delivered through six auxiliary lateral channels, selectively encapsulated the device while preserving the open interwinding channels, yielding reproducible sealing without structural collapse (Supplementary Fig. S5a). The procedure consistently produced mechanically intact and leak-free sealing across samples, without collapse of the tubular geometry. Photographs of the integrated chip confirmed robust interconnection with PTFE tubing and a compact footprint compatible with on-chip integration (Fig. 3a, right).

The device architecture allows for independent injection of fluid streams through the coaxial channels while maintaining complete isolation between compartments, as illustrated in the connection scheme (Fig. 3b). The integrity of the microfluidic architecture was confirmed through sequential filling experiments. These tests demonstrated uniform wetting of both coaxial tubes and a controlled, sequential filling of the interwinding channels (Supplementary Fig. S5b and Supplementary Videos V1–5). This progression, guided by the SU-8 spacer design, confirms efficient fluidic access to the entire 3D geometry and demonstrates the potential for localized fluidic addressing within the coiled architecture.

This robust and reproducible integration strategy combines self-assembled coaxial nanomembrane tubes with soft lithographic microfluidics, enabling precise dual-channel fluid control within a fully sealed microsystem.

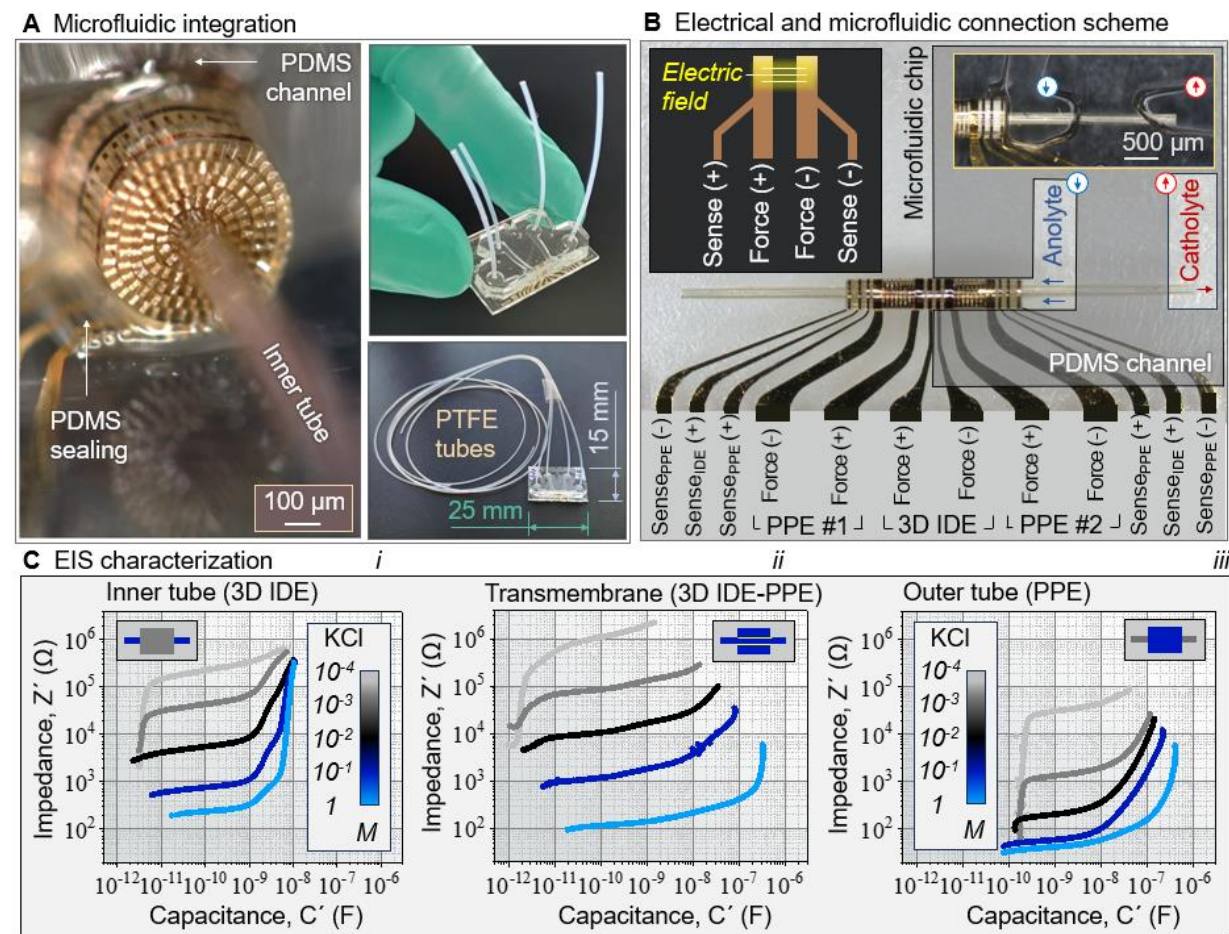


Fig. 3 Microfluidic integration and electrical characterization of the coaxial platform.

a Photographs of the device: the left image shows an open configuration with selective sealing of the inner and outer tubes, illustrating the preserved interwinding channels; the right image shows the fully assembled PDMS microfluidic chip with fluidic interconnects, **b** Electrical and microfluidic connection scheme, detailing the independent supply of fluids to the inner

(catholyte) and outer (anolyte) channels, **c** Electrochemical impedance spectroscopy (EIS) performance of the integrated electrodes across a range of KCl solutions (10^{-4} to 1 M). The data for the 3D interdigitated electrodes (IDEs, *i*), the 3D IDE–parallel-plate electrode (PPE) pair (*ii*), and the PPEs (*iii*) demonstrate that PPEs exhibit the lowest impedance, while the 3D IDEs provide stable performance across ionic strengths.

3.3 Electrical integrity and geometry-dependent electrode characterization

Electrochemical impedance spectroscopy (EIS) characterization of the integrated platform confirmed its electrical robustness, revealing low interfacial resistance and stable electrode connectivity (Fig. 3c). This validates that the self-assembly and microfluidic integration processes preserve the electrical integrity required for precise readout. To evaluate performance, EIS was conducted across KCl concentrations from 10^{-5} to 1 M (Fig. 3c, Supplementary Figs. S6–S7; Supplementary Information, Experimental Section). Capacitance–impedance spectra (C' vs. Z' , Fig. 3c) revealed distinct responses for each electrode geometry. At low ionic strength, all electrodes showed reduced capacitance, consistent with the increased thickness of the electrical double layer's diffuse region. This effect was most pronounced for planar 2D interdigitated electrodes (IDEs). Increasing ionic strength decreased the double-layer thickness, thereby increasing the measured capacitance and decreasing the impedance. Increasing ionic strength stabilized capacitance and decreased impedance. Parallel-plate electrodes (PPEs) exhibited the most extended capacitive plateau, consistent with their larger effective surface area, whereas 3D coaxial IDEs provided a broader frequency window of stable double-layer charging.

The corresponding Bode plots ($|Z|$ vs. frequency; Supplementary Fig. S7) supported these findings. 3D IDEs maintained lower impedance across the full frequency range, while PPEs exhibited suppressed impedance at intermediate to high frequencies (10^3 – 10^5 Hz), indicating enhanced charge-transfer characteristics. To probe sensitivity to dielectric environments, measurements were performed in ethanol–water mixtures (Supplementary Fig. S8). Decreasing the solvent dielectric constant increased impedance and reduced capacitance across all geometries. PPEs were most sensitive, showing nearly three orders of magnitude change in impedance at 100 Hz, while 2D IDEs remained stable and 3D IDEs displayed intermediate behaviour. This dielectric dependence aligns with double-layer theory and highlights how geometry can tailor environmental sensitivity.

Collectively, these results confirm the electrical robustness of the platform and demonstrate that electrode geometry dictates the electrochemical response. PPEs maximize interfacial area and dielectric sensitivity, while 3D IDEs provide stable charge transfer across frequencies, establishing a versatile foundation for integrated microscale electrochemical systems.

3.4 Tuning proton exchange in a multi-winding membrane architecture

The proton exchange membrane (PEM) governs ionic transport in the coaxial Swiss-roll platform and thus directly determines device performance. Fig. 4a shows a schematic cross-section of the architecture, highlighting proton transport pathways across a single polyimide (PI) membrane layer between adjacent windings, and across multiple layers between the inner and outer tubes. This multi-winding geometry creates distinct ionic conduction paths and underscores the role of membrane properties in electrochemical behaviour. SEM (Fig. 4b) resolved the winding morphology and spacer architecture, confirming uniform interwinding spacing and mechanically stable channels that act as controlled ion-conducting pathways.

Proton transfer dynamics were evaluated by introducing HCl and monitoring pH variation across membranes over time (Fig. 4c). The $\sim 1.3 \mu\text{m}$ thick PI membranes were systematically treated in NaOH, achieving resistances from $>1 \text{ M}\Omega$ (pristine) down to $\sim 250 \Omega$ after optimal conditioning. This tunability originates from a controlled hydrolysis process (Fig. 4d). The mild alkali treatment partially opens imide rings (Fig. 4d, i), introducing carboxylate and amide groups that increase hydrophilicity and create hydrated proton-conducting domains, as confirmed by FTIR spectroscopy (Supplementary Fig. S9a), thereby improving proton mobility. However, excessive hydrolysis disrupts polymer chain cohesion, leading to swelling and mechanical fragilization. This trade-off defines an optimal processing window for balancing conductivity and stability.

Consequently, moderate treatments (yielding $\sim 9 \text{ k}\Omega$ – 500Ω) (Fig. 4d, ii and Supplementary Fig. S9b) significantly improved proton transfer relative to untreated PI, while the most efficient exchange was achieved at $\sim 250 \Omega$. When compared to commercial PEMs (Fig. 4d, iii), a single optimally treated PI layer approached the performance of NafionTM 117, while additional layers slowed transport yet still outperformed KaptonTM. The balance of conductivity and mechanical robustness led us to adopt $\sim 250 \Omega$ PI membranes for subsequent device integration.

These results demonstrate that (i) proton exchange in multilayer Swiss-roll geometries can be finely tuned by the controllable treatment of individual ultrathin PI films, (ii) the platform inherently benefits from minimal local transport distances along winding interfaces, and (iii)

conductivity can be modulated over several orders of magnitude. This pre-fabrication control over a fundamental device property establishes a versatile and scalable pathway for creating bio-electronic microsystems with customized ionic pathways.

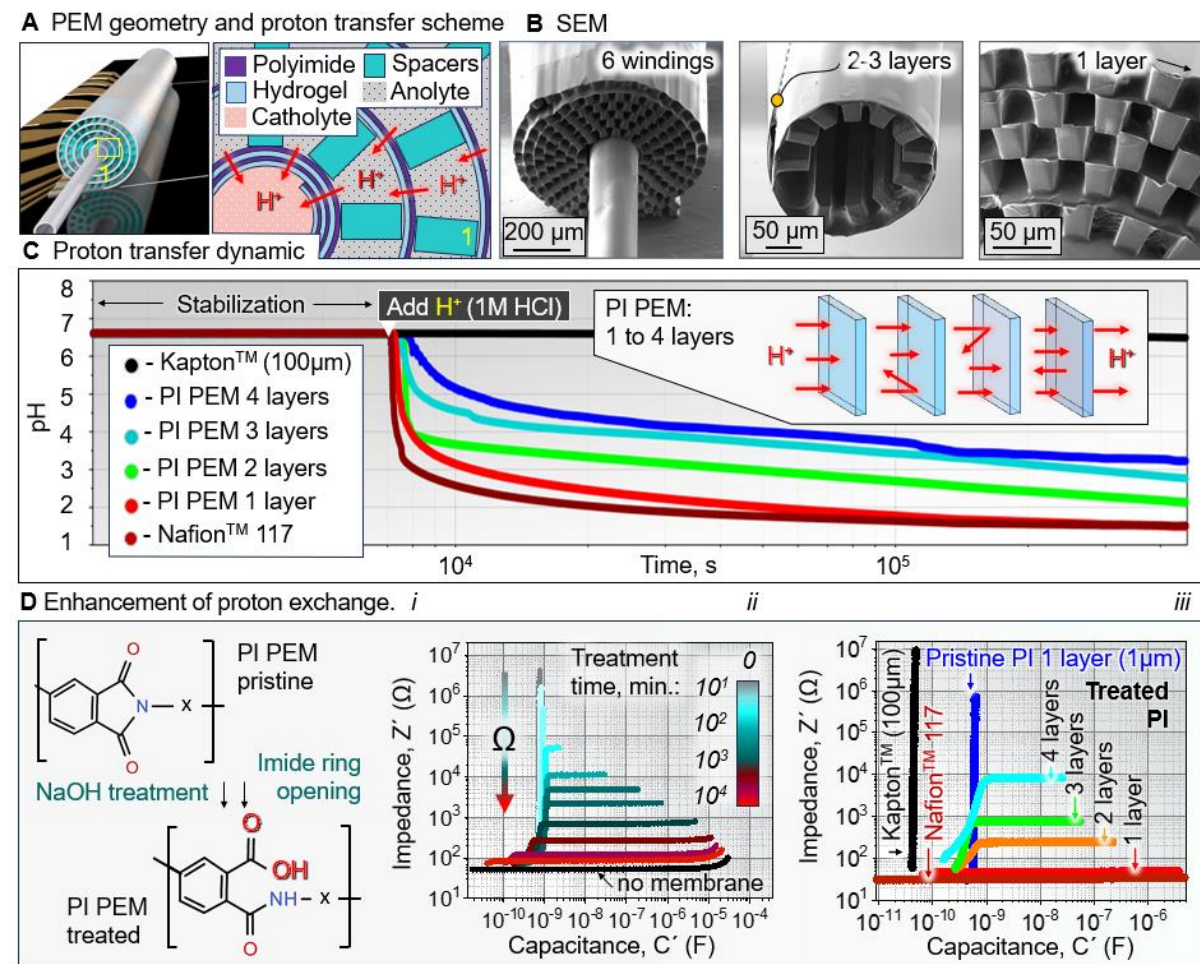


Fig. 4 Enhanced proton transport via chemically tuned polyimide membranes in the Swiss-roll architecture. **a** Schematic cross-section illustrating proton transport pathways across single and multiple polyimide (PI) membrane layers in the multi-winding geometry. **b** SEM resolving the winding morphology, showing regions with single and multiple polyimide layers (corresponding to the pathways in a) and confirming the mechanically stable, uniform interwinding spacers. **c** Proton transfer dynamics, showing pH variation over time for treated PI membranes of different layer counts (1-4 layers) compared to commercial benchmarks (Nafion™ 117, Kapton™) after H⁺ addition. **d** Chemical tuning and performance. *(i)* Mechanism of NaOH-induced hydrolysis, where partial imide ring-opening creates hydrophilic proton-conducting domains. *(ii)* Membrane resistance decreases with treatment time, defining an optimal window at ~250 Ω. *(iii)* Benchmarking shows a single tuned PI layer approaches Nafion™ 117 performance, compared to multi-layer PI stacks and Kapton™.

3.5 Component-level optimization of a bio-electrochemical energy system

To identify the key parameters governing system efficiency, we established a macro-scale model where electrodes, the proton exchange membrane (PEM), and the redox mediator could be varied independently. *Saccharomyces cerevisiae* served as the microbial catalyst, oxidizing glucose and reducing the anodic exogenous mediator methylene blue, which subsequently transferred electrons to the anode. The catholyte contained a ferri/ferrocyanide redox couple as a stable electron acceptor.

Electrode geometry emerged as a primary determinant of performance. Increasing the anodic surface area consistently raised both current density and maximum power output (Fig. 5b, *i–ii*). Large anodes ($>200 \text{ mm}^2$) supported currents above $150 \mu\text{A}$ and peak power exceeding $20 \mu\text{W}$. In contrast, enlarging the cathode provided only modest improvements. These results confirm that the anodic reaction, which is driven by mediator cycling between microbial metabolism and the electrode, is the main system bottleneck.

Performance of a macro-scale model MFC system

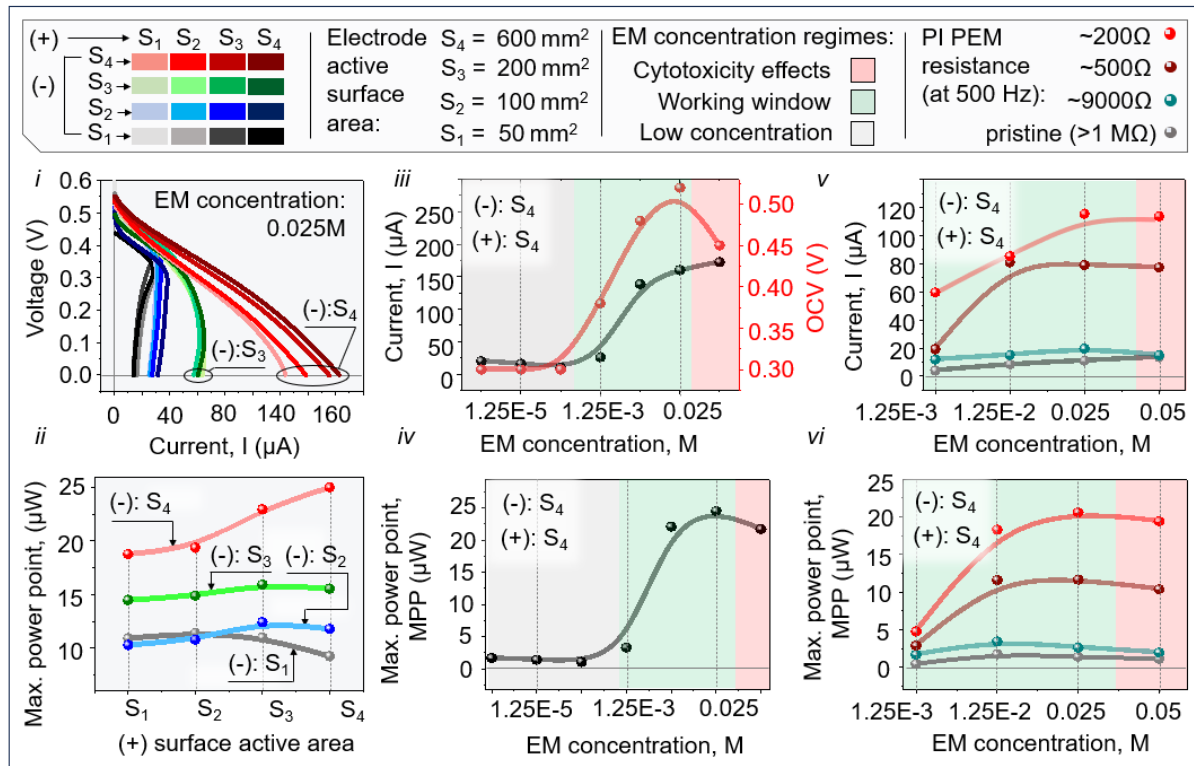


Fig. 5 Component-level optimization of the bio-electrochemical system. Influence of electrode geometry (*i–ii*), exogenous mediator (EM) concentration (*iii–iv*), and proton exchange membrane (PEM) resistance (*v–vi*) on system performance. *i–ii*, Increasing anode surface area

enhanced current and power, with large anodes ($>200\text{ mm}^2$) supporting $>150\text{ }\mu\text{A}$ and $>20\text{ }\mu\text{W}$, while cathode enlargement yielded minimal gains. *iii-iv*, Mediator concentration exhibited an optimal window ($\sim0.0125\text{--}0.025\text{ M}$); lower concentrations limited electron transfer while higher levels induced cytotoxicity. *v-vi*, PEM resistance was critical: low-resistance PI membranes ($\sim200\text{ }\Omega$) enabled high performance, whereas intermediate ($\sim500\text{ }\Omega$) and high ($\geq 9\text{ k}\Omega$) resistance severely limited output. These results establish key design rules: maximize anode area, maintain mediator within a biocompatible range, and minimize PEM resistance. Data points are measurements; lines are guides for the eye (*ii-vi*).

The concentration of the exogenous mediator defined a narrow operational window (Fig. 5b, *iii-iv*; Supplementary Fig. S10). Optimal performance was observed in the 1.25×10^{-3} to 0.025 M range, yielding power densities $>20\text{ }\mu\text{W}$ at $\sim120\text{ }\mu\text{A}$. However, very low concentrations ($<1.25\times10^{-5}\text{ M}$) failed to sustain effective electron transfer, and higher concentrations ($\geq 0.05\text{ M}$) reduced output, an effect attributed to cytotoxicity. This biphasic response highlights the critical need to balance electrochemical kinetics with biological compatibility.

The PEM exerted dominant control over overall performance (Fig. 5b, *v-vi*; Supplementary Figs. S10-S11). Untreated polyimide (PI) membranes with high resistance ($>1\text{ M}\Omega$) nearly suppressed current and power. Our tunable PI membranes, when treated to achieve low resistance ($\sim100\text{--}250\text{ }\Omega$), supported the highest performance, while intermediate ($\sim500\text{ }\Omega$) and high ($\geq 9\text{ k}\Omega$) resistance caused a marked decline. These results emphasise that PEM resistance is a critical limiting factor.

Together, these macro-scale experiments establish the key design rules for our coaxial integration: maximize anodic surface area, maintain mediator concentration within a biocompatible but electrochemically effective window ($\sim1.25\times10^{-3}\text{--}0.025\text{ M}$), and minimize PEM resistance using moderately treated PI membranes ($\sim200\text{--}250\text{ }\Omega$). These systematic, component-level insights provided a direct and universal quantitative framework for rational device design, which we applied to our coaxial Swiss-roll μMFC .

3.6 Sustainable dual-mode operation and performance benchmarking of a coaxial Swiss-roll bio-electronic platform

To demonstrate a path toward sustainable performance and circular operation, we implemented a dual-mode operational strategy for the coaxial Swiss-roll platform that integrates microbial

metabolism with mediator cycling (Fig. 6a). This concept enables the potential recycling of active species to minimize waste and facilitate long-term function. The core principle, which is the decoupling of biological regeneration from electrochemical power generation, was experimentally validated under both microbial and cell-free conditions (Fig. 6b). In the microbial mode, electroactive yeast cells oxidized glucose in an external bioreactor, reducing the soluble mediator. The reduced mediator (EM_{red}) was then delivered to the μ MFC anode to sustain power generation. In the cell-free mode, the anolyte was filtered, leaving a purified EM_{red} solution that independently powered the device. Critically, the polarization curves of both modes nearly overlapped (Fig. 6b, *i–ii*), with peak power outputs of $\sim 1.7 \mu$ W. This confirms that pre-reduced mediators alone can sustain device operation, successfully establishing the functional decoupling that is the fundamental prerequisite for a recyclable, closed-loop system.

We next evaluated the influence of PI PEM resistance on dual-mode performance. At low resistance ($\sim 100 \Omega$), the μ MFC reached current densities of $\sim 8 \mu$ A with power maxima around 2μ W (Fig. 6b, *iii–iv*). Increasing membrane resistance to $\sim 500 \Omega$ reduced output, while highly resistive membranes ($\sim 10 \text{ k}\Omega$) limited current to $\sim 1 \mu$ A with negligible power. Electrochemical impedance spectroscopy (EIS) confirmed these findings (Fig. 6b, *v–vi*), with treated PI membranes ($\sim 100\text{--}500 \Omega$) showing low, stable impedance and highly resistive membranes exhibiting transport-limited behaviour.

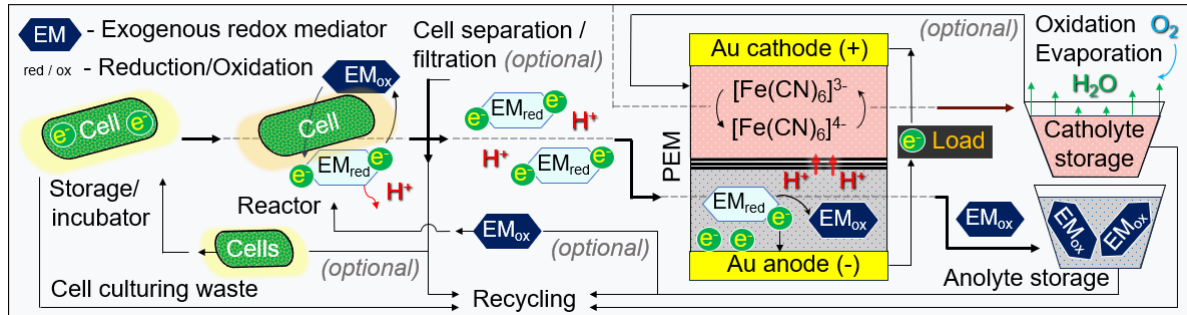
To benchmark our platform against the state of the art, we constructed a Ragone chart (Fig. 6c) comparing its performance to other reported microbial fuel cells (MFCs) with membrane-based architectures and with active electrolyte volumes below 1 mL[16,46–51]. Our coaxial Swiss-roll μ MFC achieves a unique combination of extreme miniaturization and high performance: with a footprint of only 4.16 mm^2 and a total active volume of $\sim 800 \text{ nL}$, it is, to our knowledge, the smallest membrane-based MFC reported to date, occupying less than one-sixth the area of the closest competitor. Despite this ultra-compact geometry, it delivers competitive volumetric power densities of $\sim 2.1 \text{ mW cm}^{-3}$ (total volume) and $\sim 3.1 \text{ mW cm}^{-3}$ (anode volume), positioning its performance near the upper bound of the field.

This performance stems from the 3D architecture, which decouples device footprint from electrode area. Reducing spacer size or increasing windings presents a direct route to push volumetric density further, a scaling strategy unavailable to planar designs.

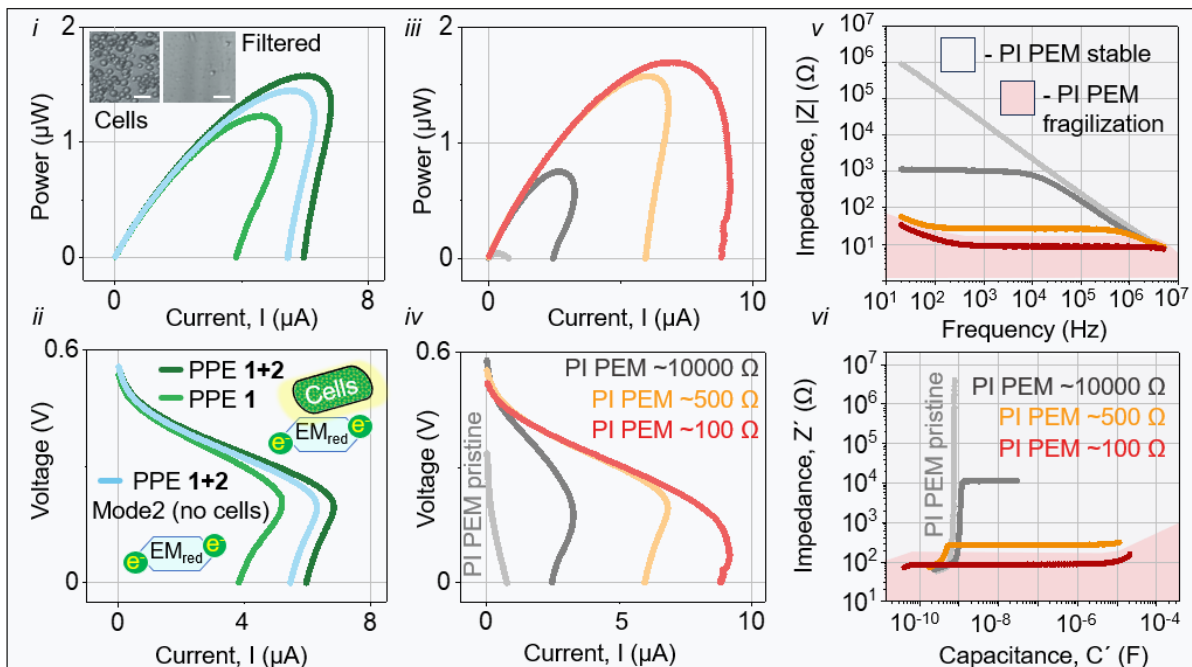
Collectively, these results validate the coaxial Swiss-roll as a foundational architecture for integrated bio-electronics. This bottom-up, self-assembly platform provides a scalable microelectronic fabrication path to creating 3D, fluidically complex systems that are otherwise

impractical to build, delivering a unique combination of ultra-small footprint, low volume, and high volumetric power density. By unifying a tunable ion-exchange membrane, high-surface-area electrodes, and a stability-enhancing operational scheme within a single monolithically integrated platform, this work moves beyond a standalone device. It establishes a versatile and integrable blueprint for powering the next generation of autonomous microsensors, advanced bio-hybrid systems, and other devices for sustainable microscale power.

A Scheme of electron transfer in anolyte through cell separation and material recirculation



B Performance of microfluidic fuel cell



C Ragone chart showing volumetric power density vs state-of-the-art microfluidic MFC

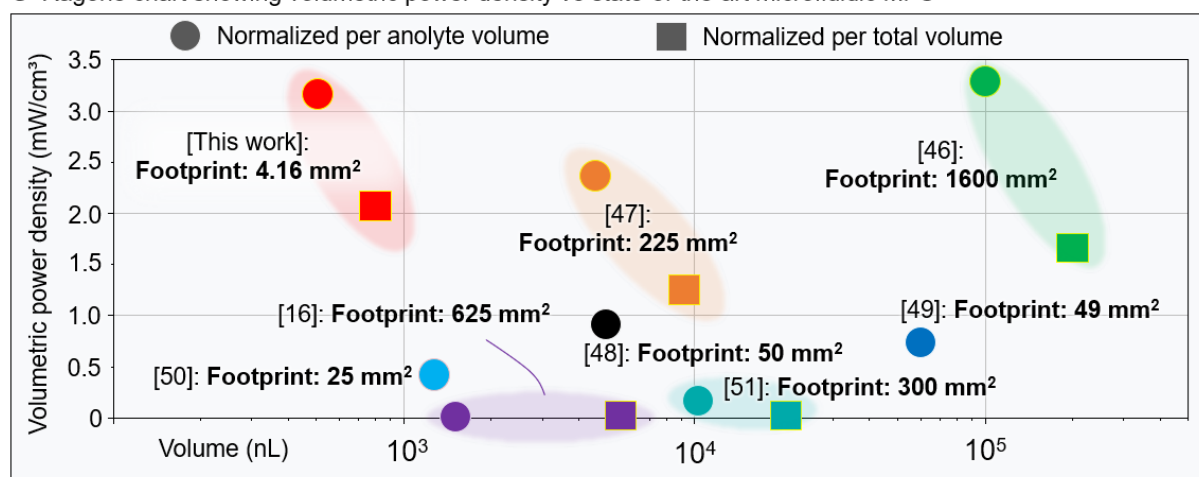


Fig. 6 Dual-mode operation and performance benchmarking of the coaxial Swiss-roll μ MFC.

a Concept of dual-mode operation. In Mode 1 (microbial), cells in an external reactor reduce the mediator, which transfers electrons to the coaxial anode while protons cross the PEM to the cathode. In Mode 2 (cell-free), cells are removed and the purified reduced mediator (EM_{red}) sustains anodic current; the oxidized mediator (EM_{ox}) can be recycled for regeneration. This

strategy enables uninterrupted operation and prevents electrode fouling. **b** Experimental validation of dual-mode operation and PEM dependence. (*i-ii*) Polarization and power density curves show cell-free operation yields power densities comparable to microbial mode, with a peak output of $\sim 1.7 \mu\text{W}$ and open-circuit voltages of 0.35–0.40 V. (*iii-iv*) PEM resistance strongly dictates performance: low-resistance PI membranes ($\sim 100 \Omega$) support currents up to $\sim 8 \mu\text{A}$ and power maxima of $\sim 2 \mu\text{W}$, intermediate resistance ($\sim 500 \Omega$) reduces output to $\sim 6 \mu\text{A}$ and $\sim 1.3 \mu\text{W}$, and high resistance ($\sim 10 \text{k}\Omega$) suppresses current to $\sim 1 \mu\text{A}$. (*v-vi*) Electrochemical impedance spectroscopy confirms stable, low impedance for membranes at $100\text{--}500 \Omega$ and dominant capacitive behavior with large phase shifts at high resistance ($\sim 10 \text{k}\Omega\text{--}1 \text{M}\Omega$), confirming transport-limited performance. **c** Performance benchmarking against the state-of-the-art [16,46–51]. Ragone chart comparing volumetric power density against electrolyte volume for membrane-based μMFCs with total volumes $< 1 \text{ mL}$. Our coaxial Swiss-roll μMFC achieves $\sim 2.1 \text{ mW cm}^{-3}$ (normalized to total volume, $\sim 800 \text{ nL}$) and $\sim 3.1 \text{ mW cm}^{-3}$ (normalized to anode volume, $\sim 550 \text{ nL}$) within a footprint of 4.16 mm^2 , ranking among the highest volumetric performers while maintaining the smallest footprint in the field.

4. Conclusion

We have demonstrated a self-assembled coaxial Swiss-roll architecture that establishes a scalable platform for integrated bio-electronic microsystems. This approach synergistically combines a bottom-up, strain-engineered 3D microfabrication process with lithographically patterned and chemically tunable polyimide proton-exchange membranes. A dual-mode operational scheme decouples microbial metabolism from on-chip power generation, enhancing stability and mitigating biofouling.

The integrated platform achieves a high degree of miniaturization, operating with a total active volume of $0.80 \mu\text{L}$ and a compact footprint of 4.16 mm^2 . It delivers volumetric power densities of $\sim 3.1 \text{ mW cm}^{-3}$, positioning it at the forefront of miniaturized bio-electrochemical power. The programmability of the membrane and the inherent scalability of the architecture provide a direct route for further performance gains through geometric tuning.

This work provides a foundational bio-electronic platform. The co-fabrication of tunable ion-conducting membranes and high-surface-area 3D microelectrodes via self-assembly opens new routes for powering autonomous microsensors and advances the development of more sophisticated and self-sustaining bio-hybrid devices.

Acknowledgements

Authors thank C. Schmidt, A. M. Placht, A. Dumler for the technical support. Authors thank Jie Lai (School of Materials Science and Engineering, Shenzhen University) for FTIR measurements. D.K. and O.G.S. acknowledge support by the German Research Foundation DFG (KA 5051/3-1 SCHM 1298/32-1). DK acknowledges Horizon Europe HORIZON-EIC-2024-PATHFINDEROPEN-01, 101186701 — LEAF. O.G.S. acknowledges DFG Leibniz Programme.

Authors' Contributions:

A.E., D.K. and O.G.S. conceived the idea and supervised the whole project. A.E., H.T. and D.D.K designed the experiment and fabricated the device. H.T., P.S. and P.F. assisted in the sample preparation, fabrication of experimental setup and testing the performance of the device. M.Z., D.K. and H.T. assisted in characterization of cell performance. A.E. and D.K. wrote paper draft. All authors discussed the results and contributed to the manuscript preparation.

Declarations

Conflict of Interest

The authors declare no competing interests

Figure and table captions

Fig. 1 Concept of the self-assembled coaxial Swiss-roll bio-electronic platform. **a** Schematic of the 3D self-assembled architecture integrated into a microfluidic system, showing the inner catholyte channel (inner tube) and the outer anolyte channel (outer tube) with integrated parallel-plate electrodes (PPEs). **b** Dual-mode operational scheme providing functional versatility. The platform supports two distinct states: a microbial mode 1 (functioning as a pure microbial fuel cell with integrated biology) and a cell-free mode 2 (operating as an abiotic electrochemical generator using pre-charged mediator). This allows the system to dynamically alternate between regenerative bio-power and stable electrochemistry, providing a robust interface between biological and electronic subsystems.

Fig. 2 Structural characterization of the self-assembled coaxial Swiss-roll microtubes. Optical microscope images of the fabricated 3D architecture after release from the substrate. The main panel shows an overview of the structure, highlighting the simultaneous formation of the inner and outer tubes. The **left** panel provides a magnified view of the SU-8 spacer bars that define the interwinding gaps and fluidic channels. The **right** panel shows a higher-magnification side view of the tube entrance, revealing the tightly packed and uniform windings that ensure mechanical stability.

Fig. 3 Microfluidic integration and electrical characterization of the coaxial platform. **a** Photographs of the device: the left image shows an open configuration with selective sealing of the inner and outer tubes, illustrating the preserved interwinding channels; the right image shows the fully assembled PDMS microfluidic chip with fluidic interconnects, **b** Electrical and microfluidic connection scheme, detailing the independent supply of fluids to the inner (catholyte) and outer (anolyte) channels, **c** Electrochemical impedance spectroscopy (EIS) performance of the integrated electrodes across a range of KCl solutions (10^{-4} to 1 M). The data for the 3D interdigitated electrodes (IDEs, *i*), the 3D IDE–parallel-plate electrode (PPE) pair (*ii*), and the PPEs (*iii*) demonstrate that PPEs exhibit the lowest impedance, while the 3D IDEs provide stable performance across ionic strengths.

Fig. 4 Enhanced proton transport via chemically tuned polyimide membranes in the Swiss-roll architecture. **a** Schematic cross-section illustrating proton transport pathways across single and multiple polyimide (PI) membrane layers in the multi-winding geometry. **b** SEM resolving the winding morphology, showing regions with single and multiple polyimide layers (corresponding to the pathways in a) and confirming the mechanically stable, uniform interwinding spacers. **c** Proton transfer dynamics, showing pH variation over time for treated PI membranes of different layer counts (1-4 layers) compared to commercial benchmarks (NafionTM 117, KaptonTM) after H⁺ addition. **d** Chemical tuning and performance. (*i*) Mechanism of NaOH-induced hydrolysis, where partial imide ring-opening creates hydrophilic proton-conducting domains. (*ii*) Membrane resistance decreases with treatment time, defining an optimal window at $\sim 250 \Omega$. (*iii*) Benchmarking shows a single tuned PI layer approaches NafionTM 117 performance, compared to multi-layer PI stacks and KaptonTM.

Fig. 5 Component-level optimization of the bio-electrochemical system. Influence of electrode geometry (*i-ii*), exogenous mediator (EM) concentration (*iii-iv*), and proton exchange membrane (PEM) resistance (*v-vi*) on system performance. *i-ii*, Increasing anode surface area enhanced current and power, with large anodes ($>200 \text{ mm}^2$) supporting $>150 \mu\text{A}$ and $>20 \mu\text{W}$, while cathode enlargement yielded minimal gains. *iii-iv*, Mediator concentration exhibited an optimal window ($\sim 0.0125\text{--}0.025 \text{ M}$); lower concentrations limited electron transfer while higher levels induced cytotoxicity. *v-vi*, PEM resistance was critical: low-resistance PI membranes ($\sim 200 \Omega$) enabled high performance, whereas intermediate ($\sim 500 \Omega$) and high ($\geq 9 \text{ k}\Omega$) resistance severely limited output. These results establish key design rules: maximize anode area, maintain mediator within a biocompatible range, and minimize PEM resistance. Data points are measurements; lines are guides for the eye. (*ii-vi*).

Fig. 6 Dual-mode operation and performance benchmarking of the coaxial Swiss-roll μ MFC. **a** Concept of dual-mode operation. In Mode 1 (microbial), cells in an external reactor reduce the mediator, which transfers electrons to the coaxial anode while protons cross the PEM to the cathode. In Mode 2 (cell-free), cells are removed and the purified reduced mediator (EM_{red}) sustains anodic current; the oxidized mediator (EM_{ox}) can be recycled for regeneration. This strategy enables uninterrupted operation and prevents electrode fouling. **b** Experimental validation of dual-mode operation and PEM dependence. (*i-ii*) Polarization and power density curves show cell-free operation yields power densities comparable to microbial mode, with a peak output of $\sim 1.7 \mu\text{W}$ and open-circuit voltages of $0.35\text{--}0.40 \text{ V}$. (*iii-iv*) PEM resistance strongly dictates performance: low-resistance PI membranes ($\sim 100 \Omega$) support currents up to $\sim 8 \mu\text{A}$ and power maxima of $\sim 2 \mu\text{W}$, intermediate resistance ($\sim 500 \Omega$) reduces output to $\sim 6 \mu\text{A}$ and $\sim 1.3 \mu\text{W}$, and high resistance ($\sim 10 \text{ k}\Omega$) suppresses current to $\sim 1 \mu\text{A}$. (*v-vi*) Electrochemical impedance spectroscopy confirms stable, low impedance for membranes at $100\text{--}500 \Omega$ and dominant capacitive behavior with large phase shifts at high resistance ($\sim 10 \text{ k}\Omega\text{--}1 \text{ M}\Omega$), confirming transport-limited performance. **c** Performance benchmarking against the state-of-the-art [16,46-51]. Ragone chart comparing volumetric power density against electrolyte volume for membrane-based μ MFCs with total volumes $<1 \text{ mL}$. Our coaxial Swiss-roll μ MFC achieves $\sim 2.1 \text{ mW cm}^{-3}$ (normalized to total volume, $\sim 800 \text{ nL}$) and $\sim 3.1 \text{ mW cm}^{-3}$ (normalized to anode volume, $\sim 550 \text{ nL}$) within a footprint of 4.16 mm^2 , ranking among the highest volumetric performers while maintaining the smallest footprint in the field.

References

- [1] L. R. Gomez Palacios, A. G. Bracamonte, Development of nano- and microdevices for the next generation of biotechnology, wearables and miniaturized instrumentation. *RSC Adv.* **12**(20), 12806–12822 (2022). <https://doi.org/10.1039/D2RA02008D>
- [2] A. T. Kutbee, R. R. Bahabry, K. O. Alamoudi, M. T. Ghoneim, M. D. Cordero, et al., Flexible and biocompatible high-performance solid-state micro-battery for implantable orthodontic system. *npj Flex. Electron.* **1**(1), 7 (2017). <https://doi.org/10.1038/s41528-017-0008-7>
- [3] J. Ni, A. Dai, Y. Yuan, L. Li, J. Lu, Three-Dimensional Microbatteries beyond Lithium Ion. *Matter* **2**(6), 1366–1376 (2020). <https://doi.org/10.1016/j.matt.2020.04.020>
- [4] C. Santoro, F. Soavi, A. Serov, C. Arbizzani, P. Atanassov, Self-powered supercapacitive microbial fuel cell: The ultimate way of boosting and harvesting power. *Biosens. Bioelectron.* **78** 229–235 (2016). <https://doi.org/10.1016/j.bios.2015.11.026>
- [5] Y. Tekle, A. Demeke, Review on microbial fuel cell. *Int. J. Eng. Technol.* **8**(November), 424–427 (2015)
- [6] J. Ma, J. Zhang, Y. Zhang, Q. Guo, T. Hu, et al., Progress on anodic modification materials and future development directions in microbial fuel cells. *J. Power Sources* **556** 232486 (2023). <https://doi.org/10.1016/j.jpowsour.2022.232486>
- [7] J. M. Moradian, Z. Fang, Y.-C. Yong, Recent advances on biomass-fueled microbial fuel cell. *Bioresour. Bioprocess.* **8**(1), 14 (2021). <https://doi.org/10.1186/s40643-021-00365-7>
- [8] Y. Cao, H. Mu, W. Liu, R. Zhang, J. Guo, et al., Electricigens in the anode of microbial fuel cells: pure cultures versus mixed communities. *Microb. Cell Fact.* **18**(1), 39 (2019). <https://doi.org/10.1186/s12934-019-1087-z>
- [9] P. Parkhey, R. Sahu, Microfluidic microbial fuel cells: Recent advancements and future prospects. *Int. J. Hydrogen Energy* **46**(4), 3105–3123 (2021). <https://doi.org/10.1016/j.ijhydene.2020.07.019>
- [10] B. E. Logan, M. J. Wallack, K. Y. Kim, W. He, Y. Feng, et al., Assessment of Microbial Fuel Cell Configurations and Power Densities. *Environ. Sci. Technol. Lett.* **2**(8), 206–214 (2015). <https://doi.org/10.1021/acs.estlett.5b00180>

[11] O. A. Ibrahim, M. Navarro-Segarra, P. Sadeghi, N. Sabaté, J. P. Esquivel, et al., Microfluidics for Electrochemical Energy Conversion. *Chem. Rev.* **122**(7), 7236–7266 (2022). <https://doi.org/10.1021/acs.chemrev.1c00499>

[12] L. Gong, M. Abbaszadeh Amirdehi, J. M. Sonawane, N. Jia, L. Torres de Oliveira, et al., Mainstreaming microfluidic microbial fuel cells: a biocompatible membrane grown *in situ* improves performance and versatility. *Lab Chip* **22**(10), 1905–1916 (2022). <https://doi.org/10.1039/D2LC00098A>

[13] M. A. Amirdehi, N. Khodaparastasarabad, H. Landari, M. P. Zarabadi, A. Miled, et al., A High-Performance Membraneless Microfluidic Microbial Fuel Cell for Stable, Long-Term Benchtop Operation Under Strong Flow. *ChemElectroChem* **7**(10), 2227–2235 (2020). <https://doi.org/10.1002/celc.202000040>

[14] W. Yang, K. K. Lee, S. Choi, A laminar-flow based microbial fuel cell array. *Sensors Actuators B Chem.* **243** 292–297 (2017). <https://doi.org/10.1016/j.snb.2016.11.155>

[15] K. Scott, Membranes and separators for microbial fuel cells. in *Microbial Electrochemical and Fuel Cells* 153–178 (Elsevier, 2016). doi:10.1016/B978-1-78242-375-1.00005-8. <https://doi.org/10.1016/B978-1-78242-375-1.00005-8>

[16] F. Qian, M. Baum, Q. Gu, D. E. Morse, A 1.5 μ L microbial fuel cell for on-chip bioelectricity generation. *Lab Chip* **9**(21), 3076 (2009). <https://doi.org/10.1039/b910586g>

[17] C. A. Machado, G. O. Brown, R. Yang, T. E. Hopkins, J. G. Pribyl, et al., Redox Flow Battery Membranes: Improving Battery Performance by Leveraging Structure–Property Relationships. *ACS Energy Lett.* **6**(1), 158–176 (2021). <https://doi.org/10.1021/acsenergylett.0c02205>

[18] D. Düerkop, H. Widdecke, C. Schilde, U. Kunz, A. Schmiemann, Polymer Membranes for All-Vanadium Redox Flow Batteries: A Review. *Membranes (Basel)*. **11**(3), 214 (2021). <https://doi.org/10.3390/membranes11030214>

[19] G. L. Soloveichik, Flow Batteries: Current Status and Trends. *Chem. Rev.* **115**(20), 11533–11558 (2015). <https://doi.org/10.1021/cr500720t>

[20] K. B. Lam, E. F. Irwin, K. E. Healy, L. Lin, Bioelectrocatalytic self-assembled thylakoids for micro-power and sensing applications. *Sensors Actuators B Chem.* **117**(2), 480–487 (2006). <https://doi.org/10.1016/j.snb.2005.12.057>

[21] K. B. Lam, E. A. Johnson, M. Chiao, L. Lin, A MEMS Photosynthetic Electrochemical Cell Powered by Subcellular Plant Photosystems. *J. Microelectromechanical Syst.* **15**(5), 1243–1250 (2006). <https://doi.org/10.1109/JMEMS.2006.880296>

[22] M. Chiao, K. B. Lam, L. Lin, Micromachined microbial and photosynthetic fuel cells. *J. Micromechanics Microengineering* **16**(12), 2547–2553 (2006). <https://doi.org/10.1088/0960-1317/16/12/005>

[23] D. Karnaushenko, T. Kang, V. K. Bandari, F. Zhu, O. G. Schmidt, 3D Self-Assembled Microelectronic Devices: Concepts, Materials, Applications. *Adv. Mater.* **1902994** 1–30 (2019). <https://doi.org/10.1002/adma.201902994>

[24] S. Liu, L. Wang, B. Zhang, B. Liu, J. Wang, et al., Novel sulfonated polyimide/polyvinyl alcohol blend membranes for vanadium redox flow battery applications. *J. Mater. Chem. A* **3**(5), 2072–2081 (2015). <https://doi.org/10.1039/C4TA05504G>

[25] X. Huang, S. Zhang, Y. Zhang, H. Zhang, X. Yang, Sulfonated polyimide/chitosan composite membranes for a vanadium redox flow battery: influence of the sulfonation degree of the sulfonated polyimide. *Polym. J.* **48**(8), 905–918 (2016). <https://doi.org/10.1038/pj.2016.42>

[26] J. Li, X. Yuan, S. Liu, Z. He, Z. Zhou, et al., A Low-Cost and High-Performance Sulfonated Polyimide Proton-Conductive Membrane for Vanadium Redox Flow/Static Batteries. *ACS Appl. Mater. Interfaces* **9**(38), 32643–32651 (2017). <https://doi.org/10.1021/acsami.7b07437>

[27] W. Xu, J. Long, J. Liu, H. Luo, H. Duan, et al., A novel porous polyimide membrane with ultrahigh chemical stability for application in vanadium redox flow battery. *Chem. Eng. J.* **428** 131203 (2022). <https://doi.org/10.1016/j.cej.2021.131203>

[28] D. Karnaushenko, N. Münzenrieder, D. D. Karnaushenko, B. Koch, A. K. Meyer, et al., Biomimetic Microelectronics for Regenerative Neuronal Cuff Implants. *Adv. Mater.* **27**(43), 6797–6805 (2015). <https://doi.org/10.1002/adma.201503696>

[29] D. D. Karnaushenko, D. Karnaushenko, D. Makarov, O. G. Schmidt, Compact helical antenna for smart implant applications. *NPG Asia Mater.* **7**(6), e188–e188 (2015). <https://doi.org/10.1038/am.2015.53>

[30] A. I. Egunov, Z. Dou, H. Karnaushenko, Dmitriy D. Franziska, N. Kretschmann, T. Z. Katja Akgün, et al., Impedimetric Microfluidic Sensor-in-a-Tube for Label-Free Immune Cell Analysis. *Small* **17**(2002549), (2021)

[31] E. Ghosh, A. I. Egunov, D. Karnaushenko, M. Medina-Sánchez, O. G. Schmidt, Self-assembled sensor-in-a-tube as a versatile tool for label-free EIS viability investigation of cervical cancer cells. *Frequenz* **76**(11–12), 729–740 (2022). <https://doi.org/10.1515/freq-2022-0090>

- [32] O. G. Schmidt, K. Eberl, Thin solid films roll up into nanotubes. *Nature* **410**(6825), 168–168 (2001). <https://doi.org/10.1038/35065525>
- [33] V. Y. Prinz, V. . Seleznev, A. . Gutakovskiy, A. . Chehovskiy, V. . Preobrazhenskii, et al., Free-standing and overgrown InGaAs/GaAs nanotubes, nanohelices and their arrays. *Phys. E Low-dimensional Syst. Nanostructures* **6**(1–4), 828–831 (2000). [https://doi.org/10.1016/S1386-9477\(99\)00249-0](https://doi.org/10.1016/S1386-9477(99)00249-0)
- [34] J. Wang, D. Karnaushenko, M. Medina-Sánchez, Y. Yin, L. Ma, et al., Three-Dimensional Microtubular Devices for Lab-on-a-Chip Sensing Applications. *ACS Sensors* **4**(6), 1476–1496 (2019). <https://doi.org/10.1021/acssensors.9b00681>
- [35] P. Lepucki, A. I. Egunov, M. Rosenkranz, R. Huber, A. Mirhajivarzaneh, et al., Self-Assembled Rolled-Up Microcoils for nL Microfluidics NMR Spectroscopy. *Adv. Mater. Technol.* **6**(1), 2000679 (2021). <https://doi.org/10.1002/admt.202000679>
- [36] A. I. Egunov, Z. Dou, D. D. Karnaushenko, F. Hebenstreit, N. Kretschmann, et al., Impedimetric Microfluidic Sensor-in-a-Tube for Label-Free Immune Cell Analysis. *Small* **17**(5), (2021). <https://doi.org/10.1002/smll.202002549>
- [37] Y. Lee, V. K. Bandari, Z. Li, M. Medina-Sánchez, M. F. Maitz, et al., Nano-biosupercapacitors enable autarkic sensor operation in blood. *Nat. Commun.* **12**(1), 4–13 (2021). <https://doi.org/10.1038/s41467-021-24863-6>
- [38] F. Gabler, D. D. Karnaushenko, D. Karnaushenko, O. G. Schmidt, Magnetic origami creates high performance micro devices. *Nat. Commun.* **10**(1), 3013 (2019). <https://doi.org/10.1038/s41467-019-10947-x>
- [39] C. N. Saggau, F. Gabler, D. D. Karnaushenko, D. Karnaushenko, L. Ma, et al., Wafer-Scale High-Quality Microtubular Devices Fabricated via Dry-Etching for Optical and Microelectronic Applications. *Adv. Mater.* **32**(37), 2003252 (2020). <https://doi.org/10.1002/adma.202003252>
- [40] F. Li, J. Wang, L. Liu, J. Qu, Y. Li, et al., Self-Assembled Flexible and Integratable 3D Microtubular Asymmetric Supercapacitors. *Adv. Sci.* **6**(20), 1901051 (2019). <https://doi.org/10.1002/advs.201901051>
- [41] Z. Qu, M. Zhu, Y. Yin, Y. Huang, H. Tang, et al., A Sub-Square-Millimeter Microbattery with Milliampere-Hour-Level Footprint Capacity. *Adv. Energy Mater.* **12**(28), 2200714 (2022). <https://doi.org/10.1002/aenm.202200714>
- [42] H. Tang, L. M. M. Ferro, D. D. Karnaushenko, O. Selyshchev, X. Wang, et al., An “Ion Harvester” Battery in Soil Empowered by a Microfluidic Pump and Interlayer

Confinement within Micro-Swiss-Rolls. *Adv. Funct. Mater.* **35**(14), (2025). <https://doi.org/10.1002/adfm.202418872>

[43] M. Zhu, J. Hu, Q. Lu, H. Dong, D. D. Karnaushenko, et al., A Patternable and In Situ Formed Polymeric Zinc Blanket for a Reversible Zinc Anode in a Skin-Mountable Microbattery. *Adv. Mater.* **33**(8), 2007497 (2021). <https://doi.org/10.1002/adma.202007497>

[44] D. Karnaushenko, T. Kang, O. G. Schmidt, Shapeable Material Technologies for 3D Self-Assembly of Mesoscale Electronics. *Adv. Mater. Technol.* **4**(4), 1–29 (2019). <https://doi.org/10.1002/admt.201800692>

[45] X. Lai, M. Yang, H. Wu, D. Li, Modular Microfluidics: Current Status and Future Prospects. *Micromachines* **13**(8), 1–22 (2022). <https://doi.org/10.3390/mi13081363>

[46] H. Ren, C. I. Torres, P. Parameswaran, B. E. Rittmann, J. Chae, Improved current and power density with a micro-scale microbial fuel cell due to a small characteristic length. *Biosens. Bioelectron.* **61** 587–592 (2014). <https://doi.org/10.1016/j.bios.2014.05.037>

[47] S. Choi, H.-S. Lee, Y. Yang, P. Parameswaran, C. I. Torres, et al., A μ L-scale micromachined microbial fuel cell having high power density. *Lab Chip* **11**(6), 1110 (2011). <https://doi.org/10.1039/c0lc00494d>

[48] D. Vigolo, T. T. Al-Housseiny, Y. Shen, F. O. Akinlawon, S. T. Al-Housseiny, et al., Flow dependent performance of microfluidic microbial fuel cells. *Phys. Chem. Chem. Phys.* **16**(24), 12535 (2014). <https://doi.org/10.1039/c4cp01086h>

[49] H. Jiang, M. A. Ali, Z. Xu, L. J. Halverson, L. Dong, Integrated Microfluidic Flow-Through Microbial Fuel Cells. *Sci. Rep.* **7**(1), 41208 (2017). <https://doi.org/10.1038/srep41208>

[50] J. E. Mink, J. P. Rojas, B. E. Logan, M. M. Hussain, Vertically Grown Multiwalled Carbon Nanotube Anode and Nickel Silicide Integrated High Performance Microsized (1.25 μ L) Microbial Fuel Cell. *Nano Lett.* **12**(2), 791–795 (2012). <https://doi.org/10.1021/nl203801h>

[51] B. Şen-Doğan, M. Okan, N. Afşar-Erkal, E. Özgür, Ö. Zorlu, et al., Enhancement of the Start-Up Time for Microliter-Scale Microbial Fuel Cells (μ MFCs) via the Surface Modification of Gold Electrodes. *Micromachines* **11**(7), 703 (2020). <https://doi.org/10.3390/mi11070703>

Supporting materials

Thin-Film-Engineered Self-Assembly of 3D Coaxial Microfluidics with a Tunable Polyimide Membrane for Bioelectronic Power

Aleksandr I. Egunov^{1*}, Hongmei Tang¹, Pablo E. Saenz¹, Dmitriy D. Karnaushenko¹, Yumin Luo^{1,2}, Chao Zhong³, Xinyu Wang³, Yang Huang⁴, Pavel Fedorov¹, Minshen Zhu^{1*}, Daniil Karnaushenko^{1*} and Oliver, G. Schmidt^{1,5,6*}

¹ Research Center for Materials, Architectures and Integration of Nanomembranes, Chemnitz University of Technology, Chemnitz, Germany.

² Chair of Microsystems Technology, Ruhr University Bochum, Bochum, Germany

³ Shenzhen Key Laboratory of Materials Synthetic Biology, Key Laboratory of Quantitative Synthetic Biology, Shenzhen Institute of Synthetic Biology, Shenzhen Institutes of Advanced Technology, Chinese Academy of Sciences, Shenzhen, China.

⁴ Department of Physics and Materials Science, City University of Hong Kong, Hong Kong, China.

⁵ Material Systems for Nanoelectronics, Chemnitz University of Technology, Chemnitz, Germany

⁶ Nanophysics, Dresden University of Technology, Dresden, Germany

*Corresponding authors

E-mail: aleksandr.egunov@main.tu-chemnitz.de,

E-mail: minshen.zhu@main.tu-chemnitz.de,

E-mail: daniil.karnaushenko@main.tu-chemnitz.de,

E-mail: oliver.schmidt@main.tu-chemnitz.de.

Supplementary information

Extended data for Fig. 3, S6 and S7

The observed impedance and capacitance behavior (Fig. S6) can be directly explained by the physics of electric double-layer (EDL) formation. At low ionic strength (10^{-5} – 10^{-3} M KCl), the Debye screening length (λ_D) is extended, reaching ~ 100 nm at 10^{-5} M and ~ 10 nm at 10^{-3} M. In this regime, counterion accumulation at the electrode is incomplete, resulting in low double-layer capacitance and high impedance. This effect is particularly pronounced in 2D IDEs, where limited effective surface area and larger inter-electrode distances restrict efficient charge compensation.

At intermediate concentrations (10^{-2} – 10^{-1} M), λ_D contracts to ~ 3 – 1 nm, enabling more effective EDL charging and a marked increase in capacitance. In this range, the coaxial geometry of 3D IDEs provides a decisive advantage: the increased interfacial area and shortened ionic pathways reduce impedance significantly compared to 2D IDEs. PPEs, by contrast, offer extended planar interfaces that sustain strong and uniform EDL formation, leading to the lowest observed impedance across the frequency range.

At high ionic strength (1 M KCl), λ_D falls below 1 nm, producing saturated double-layer capacitance at all electrode types. Here, impedance is dominated by bulk electrolyte conductivity, and the performance gap between electrode architectures diminishes. Nonetheless, PPEs maintain the most stable capacitive response, while 3D IDEs preserve broader frequency-dependent charge storage capacity.

These findings confirm that coaxial self-rolled electrodes provide favorable conditions for EDL formation across a broad concentration range, combining low impedance with stable capacitive behavior. Such characteristics are critical for microbial fuel cell operation, where efficient charge transfer and minimized resistive losses directly translate into improved bioelectrochemical performance.

Ionic strength dependence (KCl solutions, Fig. 3c and Fig. S6).

At 1 M KCl, PPEs exhibited impedance values as low as $\sim 1.5 \times 10^3$ Ω at 100 Hz, compared to $\sim 1 \times 10^5$ Ω for 2D IDEs and $\sim 1 \times 10^4$ Ω for 3D IDEs. At lower concentration (10^{-5} M KCl), impedance increased to $\sim 5 \times 10^6$ Ω for 2D IDEs, $\sim 1 \times 10^6$ Ω for 3D IDEs, and $\sim 3 \times 10^5$ Ω for PPEs.

This reduction can be described by the classical Debye screening relation:

$$\lambda_D = \sqrt{\frac{\epsilon k_B T}{2 N_A e^2 I}}$$

where λ_D is the Debye length, ϵ is the dielectric permittivity of water ($\epsilon \approx 80$), k_B is Boltzmann constant = $1.380 \times 10^{-23} \text{ J}\cdot\text{K}^{-1}$, T — Absolute temperature, assumed 298 K (25 °C), N_A — Avogadro's number = $6.022 \times 10^{23} \text{ mol}^{-1}$, I — Ionic strength ($\text{mol}\cdot\text{L}^{-1}$), defined as

$$I = \frac{1}{2} \sum C_i Z_i^2$$

where C_i is molar concentration of ion i , and Z_i its valence.

Increasing I from 10^{-5} M to 1 M reduces λ_D from $\sim 100 \text{ nm}$ to $\sim 0.3 \text{ nm}$, explaining the improved charge screening and lowered impedance. Capacitance estimates from the Z' – C' plots confirm this: PPEs reach $\sim 3 \times 10^{-9} \text{ F}$ at 1 M KCl , compared to $\sim 2 \times 10^{-10} \text{ F}$ for 2D IDEs under the same conditions.

2. Dielectric dependence (ethanol–water mixtures, Fig. S7).

At fixed ionic content, decreasing the solvent dielectric constant from $\epsilon \approx 80$ (pure water) to $\epsilon \approx 25$ (pure ethanol) systematically increased impedance. For PPEs, $|Z|$ at 100 Hz rose from $\sim 1 \times 10^4 \Omega$ (water) to $\sim 1 \times 10^7 \Omega$ (ethanol), i.e. a three-order-of-magnitude shift.

The capacitance followed the expected scaling:

$$C \sim \frac{\epsilon}{\lambda_D}$$

where λ_D remains constant at fixed ionic concentration. This results in a direct proportionality of capacitance with ϵ . Experimentally, PPE capacitance decreased from $\sim 2 \times 10^{-9} \text{ F}$ (water) to $\sim 7 \times 10^{-11} \text{ F}$ (ethanol).

2D IDEs displayed smaller changes ($\sim 1 \times 10^{-10} \text{ F}$ to $\sim 5 \times 10^{-11} \text{ F}$) because of their strongly localized field lines, while 3D IDEs showed intermediate sensitivity.

Extended data for Fig. S8

Proton exchange in alkali-treated polyimide membranes

The alkali (NaOH) treatment of PI PEM partially hydrolyzes the imide rings of polyimide (PI) into their open-chain poly(amic acid) form. This transformation introduces carboxylate ($-\text{COO}^-$) and amide ($-\text{CONH}-$) groups that enhance ionic transport and water affinity, beneficial for proton conduction. The reaction proceeds via nucleophilic attack of hydroxide ions on the imide carbonyl carbon, followed by ring-opening to yield amic acid intermediates.

In the FTIR spectra (Fig. S9a), pristine PI shows characteristic imide peaks at:

1775 cm⁻¹ (C=O asymmetric stretch)

1720 cm⁻¹ (C=O symmetric stretch)

1380 cm⁻¹ (C–N stretch)

720 cm⁻¹ (imide ring deformation)

After NaOH exposure, new and shifted features appear:

Broad O–H/N–H stretching (3200–3600 cm⁻¹): from hydroxyl and amide groups in poly(amic acid).

Weakened imide C=O peaks (1775 and 1720 cm⁻¹): indicating ring cleavage.

New amide C=O band (~1650 cm⁻¹): characteristic of amic acid formation.

New COO⁻ symmetric stretching (~1420 cm⁻¹): confirming partial conversion to carboxylate.

The improvement in ionic transport after alkali treatment is consistent with hydrolysis of imide groups in PI:



The repeat unit of the PI contains two imide linkages per monomer, which are the primary sites for hydroxide attack. Controlled NaOH hydrolysis converts a fraction of imide rings into poly(amic)-like structures bearing amide and carboxylate/carboxylic groups. In FTIR this is manifested by a reduced and broadened imide C=O envelope (~1775 and 1720 cm⁻¹), a shoulder/increase around ~1650 cm⁻¹ (amide C=O / amic acid), increased O–H/N–H absorption (~3400 cm⁻¹), and modest growth near 1420 cm⁻¹ (COO⁻ symmetric). Excessive hydrolysis produces a high density of hydrophilic groups, causing strong swelling, gelation and partial dissolution in aqueous media — a condition we avoid by selecting an intermediate target resistance (~250 Ω at 10³ Hz).

Electrochemical impedance spectroscopy (EIS) was used to quantify membrane resistance as a function of alkali treatment time. The total impedance is represented as

$$\mathbf{Z}(\omega) \approx \mathbf{Z}'(\omega) + j\mathbf{Z}''(\omega)$$

where $Z'(\omega)$ is the real component (resistive contribution) and $Z''(\omega)$ is the imaginary component (capacitive contribution). For thin membranes, the dominant parameter is the real resistance at mid frequencies (10²–10⁴ Hz), where electrode polarization is negligible and bulk ionic conduction dominates.

The membrane resistance was extracted from the Bode plot at 10³ Hz,

$$R_{mem} \approx Z'(\omega = 10^3 \text{ Hz})$$

giving values of $\sim 10^6 \Omega$ for pristine PI, $\sim 10^5 \Omega$ after 10² min of NaOH treatment, and $\sim 10^3 \Omega$ after 10³ min (Fig. S9b). At very long treatment times ($> 7.5 \times 10^3$ min), R_{mem} increased again due to membrane fragilisation and partial loss of structural integrity.

While NafionTM 117 exhibited the lowest resistance ($\sim 10^2 \Omega$), treated PI reached comparable performance at optimal treatment times (10³–5x10³ min), with a significant mechanical advantage in multilayer coaxial integration. In contrast, KaptonTM remained insulating with $R_{mem} > 10^7 \Omega$.

Thus, alkali-treated PI provides a tunable balance between ionic conductivity and structural robustness, making it particularly suited for Swiss-roll μ MFC architectures where membrane winding introduces regions of reduced effective thickness.

Supplementary Figs. 1–11

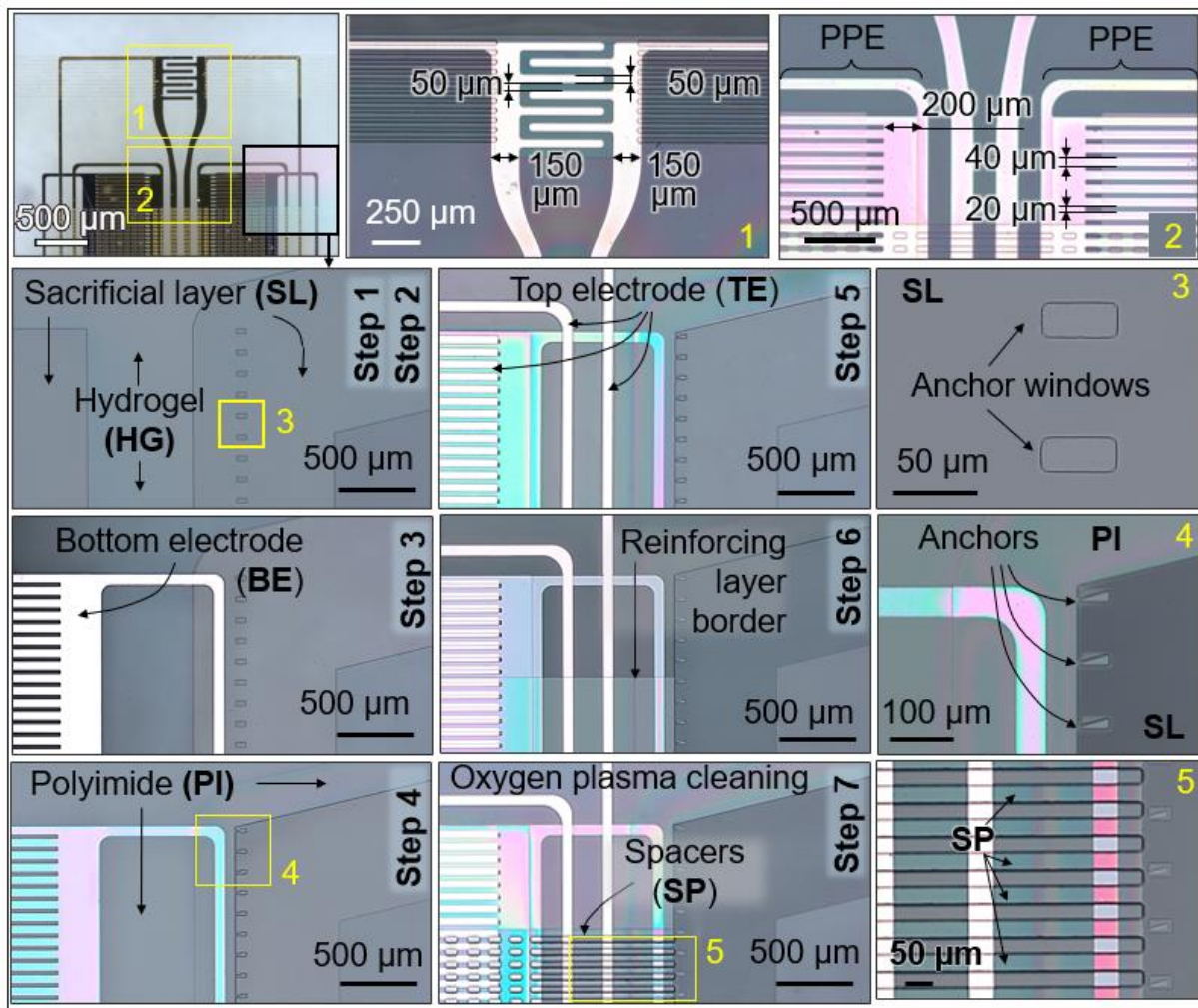


Fig. S1 Detailed microfabrication sequence. Step-by-step photolithographic process for the polymeric nanomembrane stack: (Step 1) Sacrificial layer (SL) patterning. (Step 2) Hydrogel (HG) deposition and patterning. (Step 3) Sputtering and patterning of the bottom electrode (BE, Cr/Au). (Step 4) Spin-coating and patterning of the first polyimide (PI) layer. (Step 5) Sputtering and patterning of the top electrode (TE, Cr/Au). (Step 6) Deposition and patterning of a thicker PI reinforcing layer for mechanical stability. (Step 7) Oxygen plasma cleaning and final deposition/patterning of SU-8 spacer (SP) bars. Insets 1, 2: Detailed dimensions of the electrode structures. Insets 3, 4: Design and integration of lithographic anchors to prevent lateral rolling. Inset 5: Close-up view of the SU-8 spacer bars.

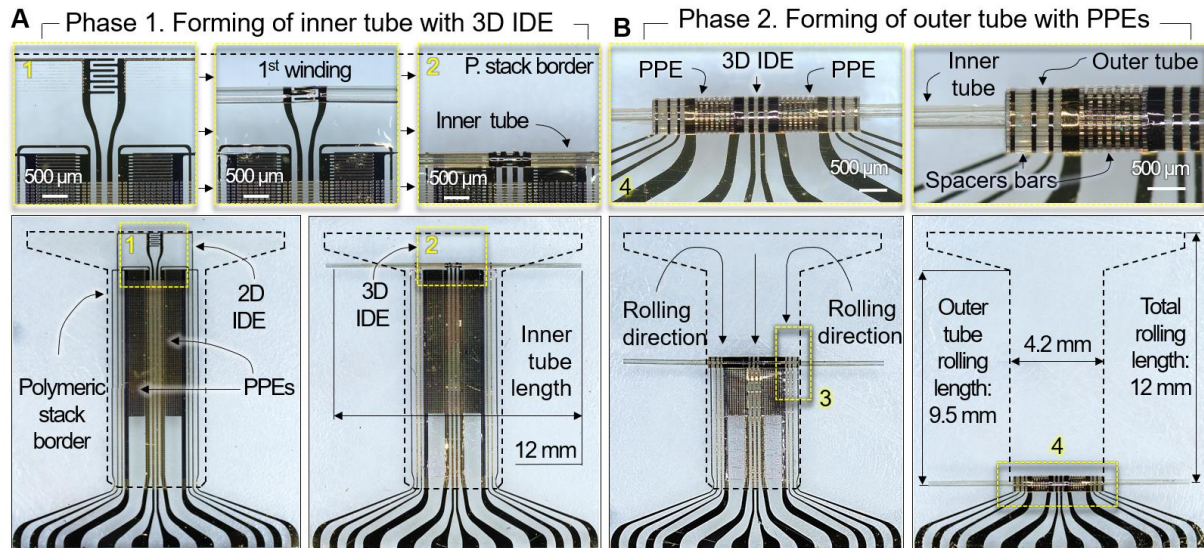


Fig. S2 Sequential self-assembly of the 3D coaxial architecture. The strain-driven rolling process occurs in two distinct phases, guided by lithographic anchors and a polyimide (PI) reinforcing layer to ensure the correct sequence. **a** Phase 1: Inner tube formation. Overview image and corresponding zoomed views (Insets 1, 2) showing the initial rolling stage that transforms the 2D interdigitated electrodes (IDEs) into the 3D inner tube. **b** Phase 2: Outer tube formation. Overview image and corresponding zoomed views (Insets 3, 4) showing the subsequent rolling stage, where the outer structure encases the inner tube to form the complete coaxial architecture with integrated parallel-plate electrodes (PPEs). The final device has a total length of 12 mm.

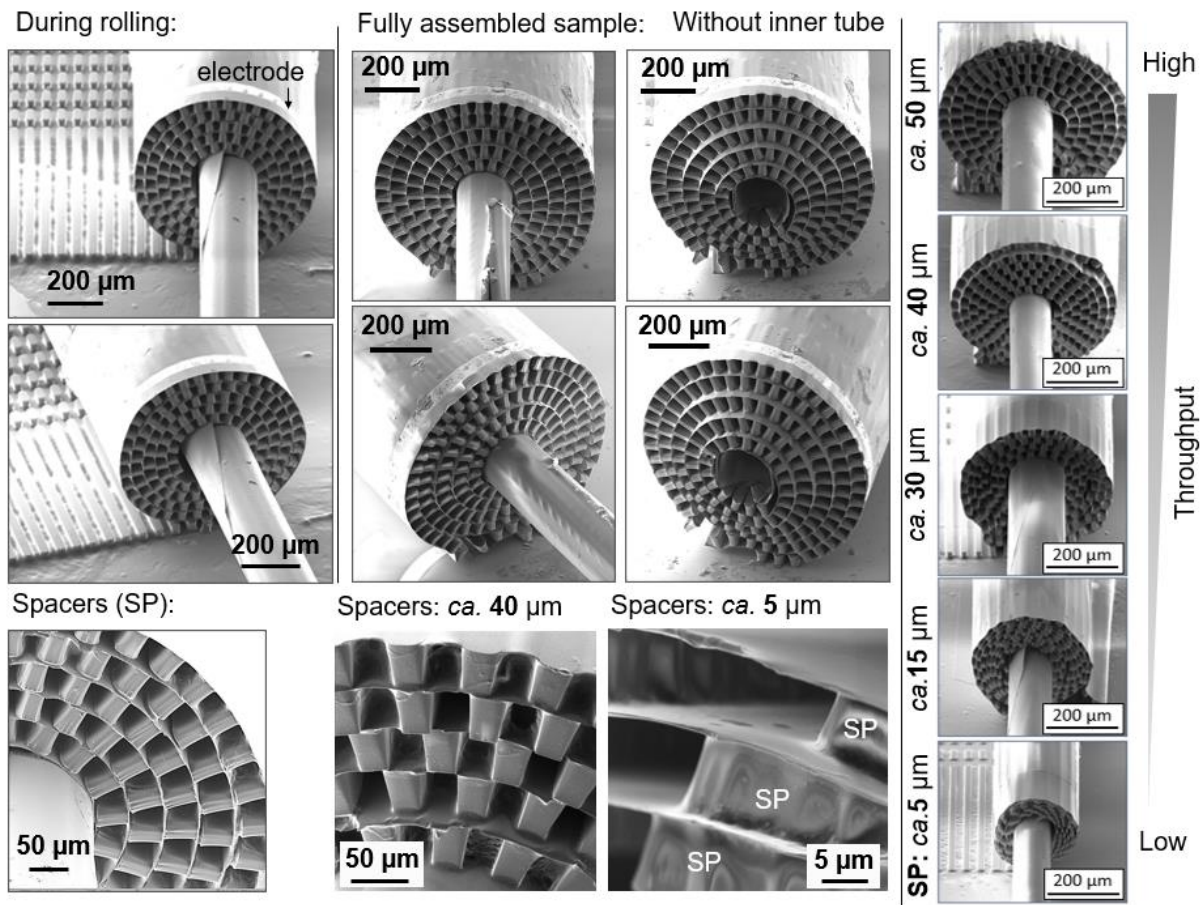


Fig. S3 Scanning electron microscopy (SEM) images of self-assembled Swiss-roll coaxial platform with varying interwinding gaps. The top row shows the fabrication process, illustrating the rolling of a layered structure into a coaxial configuration (left), resulting in the fully assembled samples (centre). The fully assembled samples exhibit a consistent pattern of concentric rings around a central inner tube, with the interwinding gap (spacer) distance systematically varied (right). The bottom rows show higher magnification views of the spacers for samples with ca. 40 μm and ca. 5 μm gaps, respectively, highlighting the microstructural morphology. The right column presents a series of fully assembled samples with varying interwinding gaps: 5 μm (volume of outer tube is \sim 70 nL), 15 μm (volume of outer tube is \sim 200 nL), 30 μm (volume of outer tube is \sim 400 nL), 40 μm (volume of outer tube is \sim 550 nL), and 50 μm (volume of outer tube is \sim 700 nL), demonstrating a clear correlation between the spacer size and the resulting macroscopic structure. The gradient bar on the right indicates the relative throughput associated with each spacer size, with larger gaps yielding higher throughput.

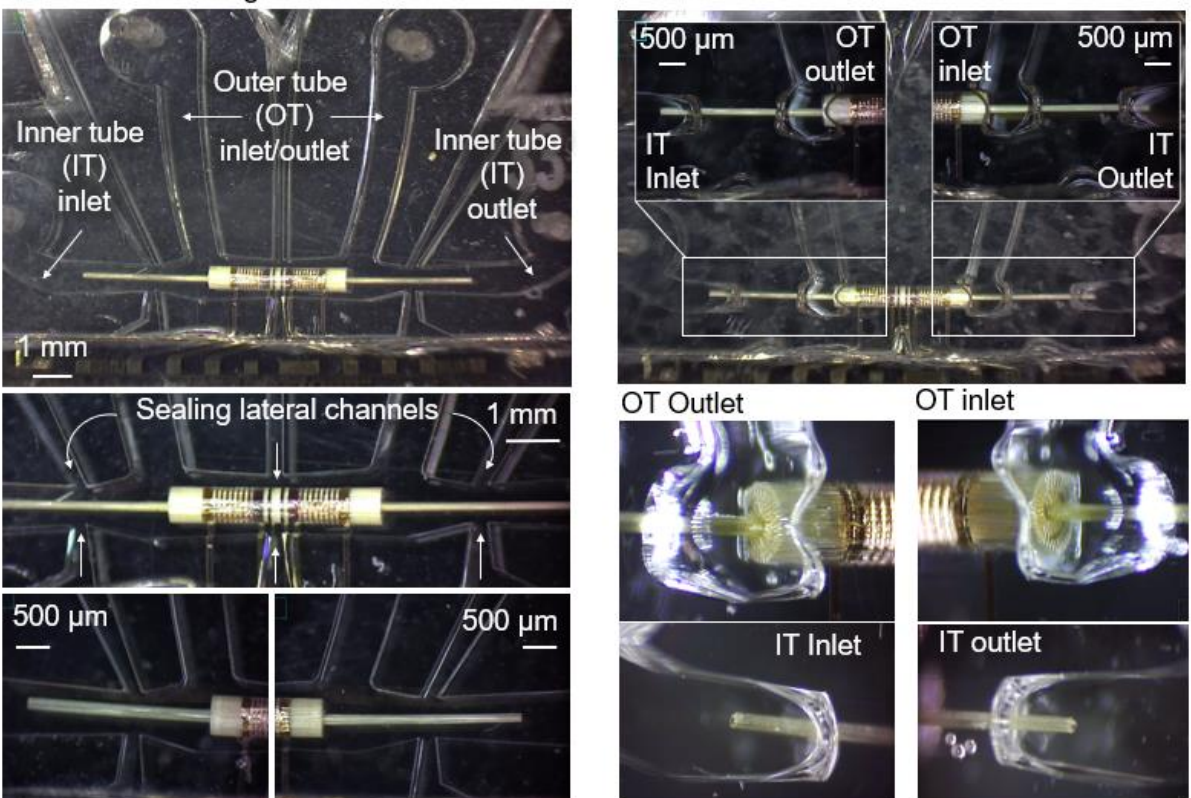
A Microfluidic integration**B Sequential laminar flow filling**

Fig. S4 Microfluidic integration and sealing of the 3D coaxial platform. **a** Sealing strategy. Optical micrographs showing the integration of the self-assembled coaxial structure within the PDMS device. The architecture is aligned in the main channel, and liquid PDMS is introduced through lateral channels to locally seal the structure, establishing isolated fluidic connections. **b** Programmable sequential filling. A series of optical micrographs demonstrating controlled, winding-by-winding fluid progression through the 3D architecture. The SU-8 spacer design creates discrete microfluidic channels within the windings, enabling precise control over the filled volume. This confirms the design provides addressable microfluidic access to the entire active surface area. Scale bars 50 μ m.

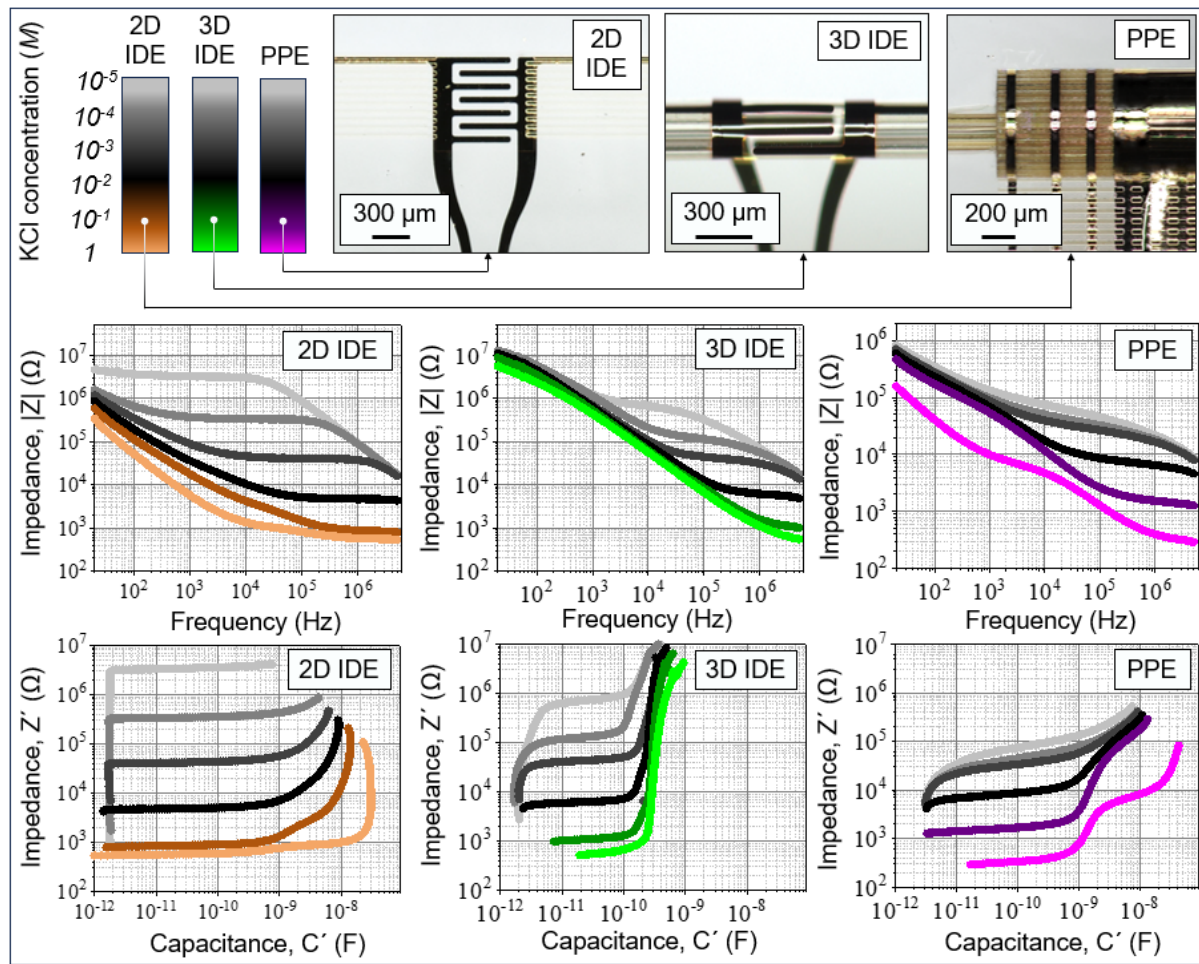


Fig. S5 Geometry-dependent electrochemical performance of the integrated electrodes. Bode plots (top row, impedance magnitude $|Z|$ vs. frequency) and capacitance spectra (bottom row) directly compare the three electrode geometries - planar 2D IDEs, 3D coaxial IDEs, and PPEs - across KCl solutions (10⁻⁵ to 1 M). The data reveal a pronounced geometry effect: the 3D self-assembled structures (3D IDEs, PPEs) consistently outperform the 2D baseline, with PPEs providing the lowest impedance and most stable capacitance due to their large surface area, while 3D IDEs offer robust performance across all ionic strengths.

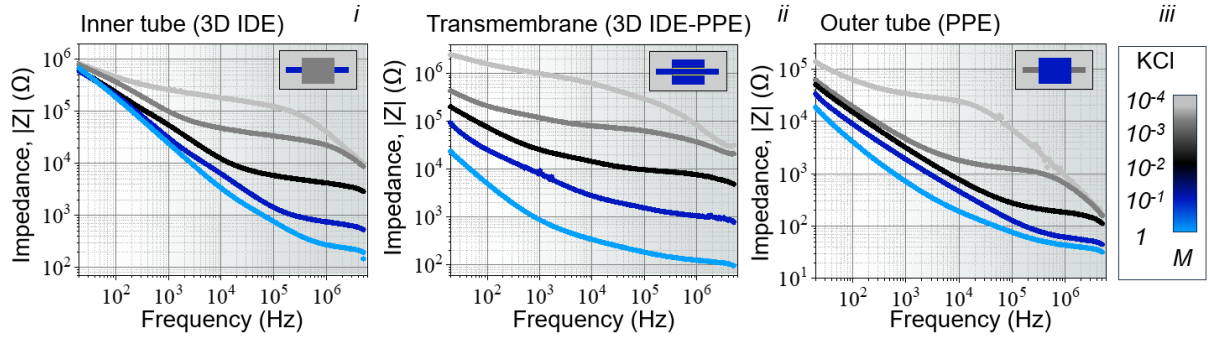


Fig. S6 Bode plot analysis corresponding to Fig. 3c. Impedance magnitude ($|Z|$) versus frequency for the same measurements shown in the capacitance–impedance plots of Fig. 3c, featuring (i) 3D IDEs, (ii) 3D IDE-PPE pair, and (iii) PPEs across KCl solutions (10^{-4} to 1 M). These Bode plots provide complementary frequency-domain analysis, quantitatively showing that PPEs maintain the lowest impedance magnitude across most frequencies, while 3D IDEs offer stable performance over the broadest frequency range.

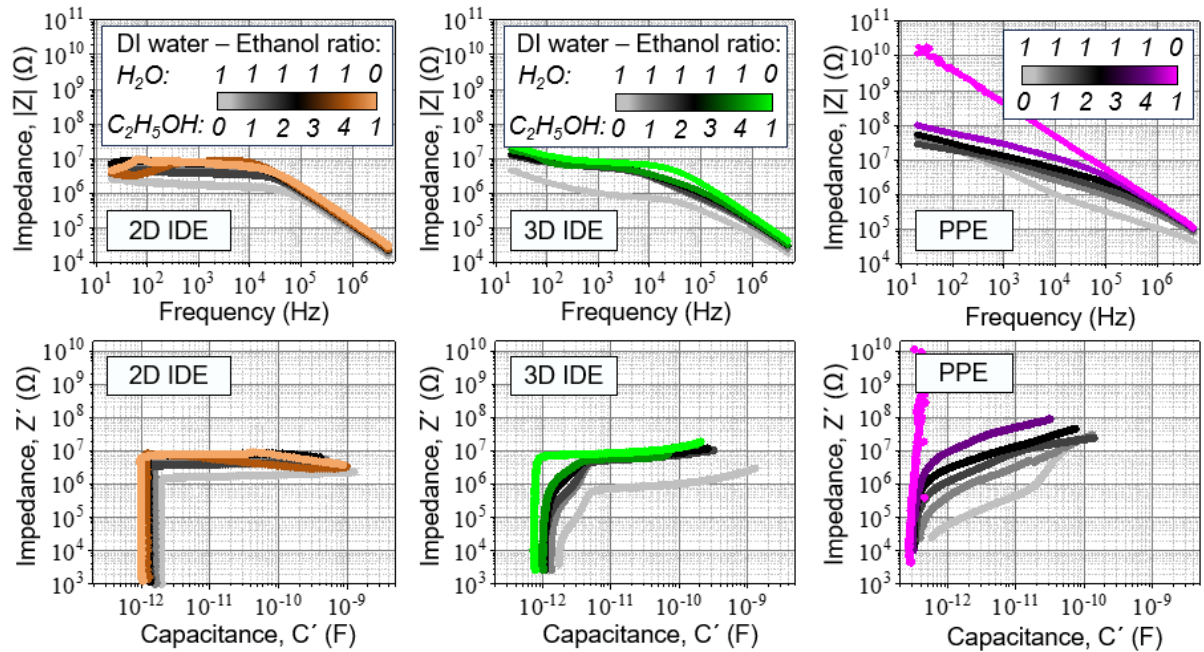
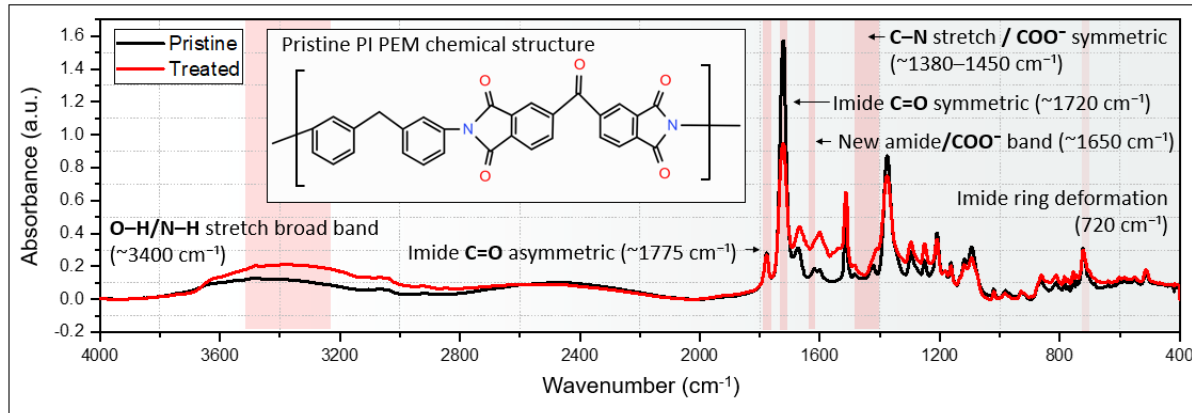


Fig. S7 Dielectric sensitivity of electrode geometries. Bode plots (top row) and corresponding capacitance spectra (bottom row) for the 2D IDEs, 3D IDEs, and PPEs in ethanol–water mixtures of varying composition (pure water to pure ethanol). The data quantify the geometry-dependent dielectric response: PPEs act as highly sensitive dielectric sensors, with impedance varying by nearly three orders of magnitude, while the IDE geometries provide stable performance, making them robust for fluctuating environments. This demonstrates the capability to select electrode geometry based on the required application, whether sensing or stable operation.

A FTIR characterization and structural scheme of PI PEM upon controlled alkali treatment



B EIS characterization of PEM

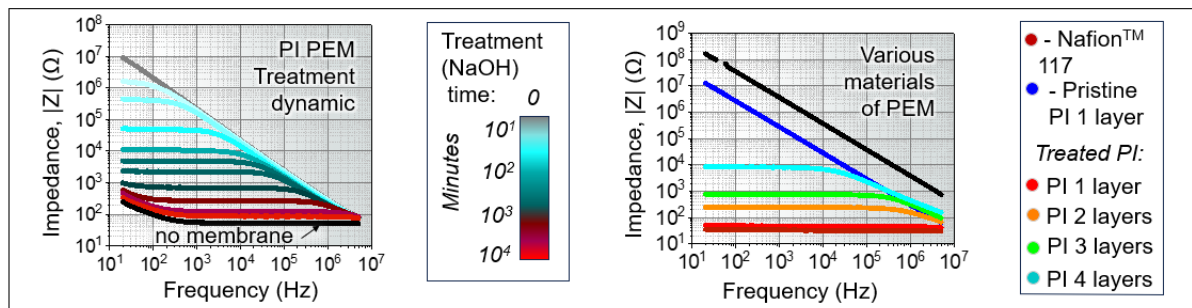
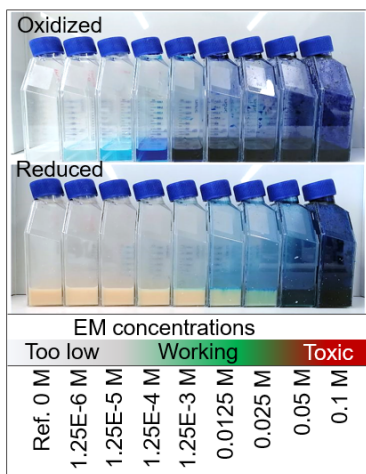


Fig. S8 Chemical and electrochemical evidence for PI PEM tunability. **a** FTIR spectra of pristine (black) and NaOH-treated (red) PI membranes. The treatment reduces characteristic imide peaks (asymmetric C=O stretch at $\sim 1775 \text{ cm}^{-1}$, symmetric at $\sim 1720 \text{ cm}^{-1}$) and introduces new bands (broad O–H/N–H at $3200\text{--}3600 \text{ cm}^{-1}$, amide C=O at $\sim 1650 \text{ cm}^{-1}$, COO^- at $\sim 1420 \text{ cm}^{-1}$), confirming the partial ring-opening into poly(amic acid) and carboxylate species that enhance hydrophilicity and proton conduction. **b** Electrochemical impedance spectroscopy (Bode plots, $|Z|$ vs. frequency) provides the underlying data for the performance metrics in Fig. 4d. The plots show the systematic reduction of membrane resistance with NaOH treatment time (left, corresponding to Fig. 4d, ii) and benchmark the performance of the optimally treated PI against commercial standards (right, corresponding to Fig. 4d, iii).

A EM concentrations optimization



B Influence of EM concentrations on MFC performance

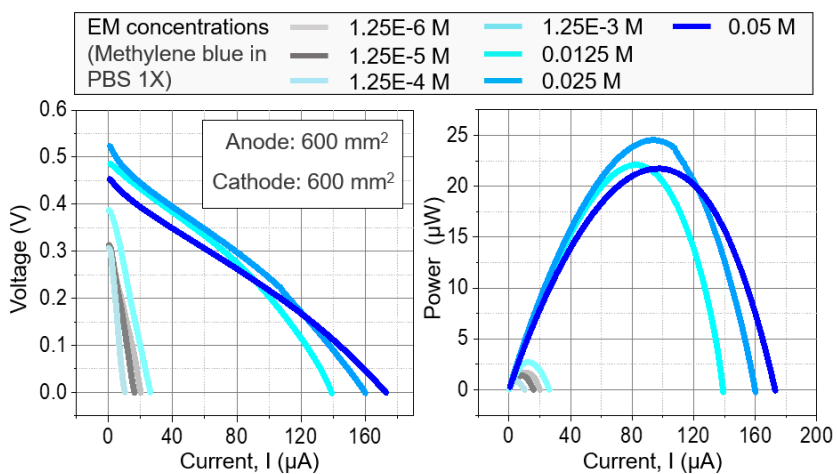


Fig. S9 Influence of exogenous mediator concentration on system performance. **a** Photographs of methylene blue solutions, showing the oxidized (blue, top) and reduced (colorless, bottom) states across a concentration gradient. The visible color transition confirms active redox cycling within the operational range. **b** Polarization and power density curves quantifying the performance window. Optimal output occurs at mediator concentrations of 1.25×10^{-3} M to 0.025 M. Performance declines at lower concentrations due to insufficient electron transfer and at higher concentrations (≥ 0.05 M) due to cytotoxic effects.

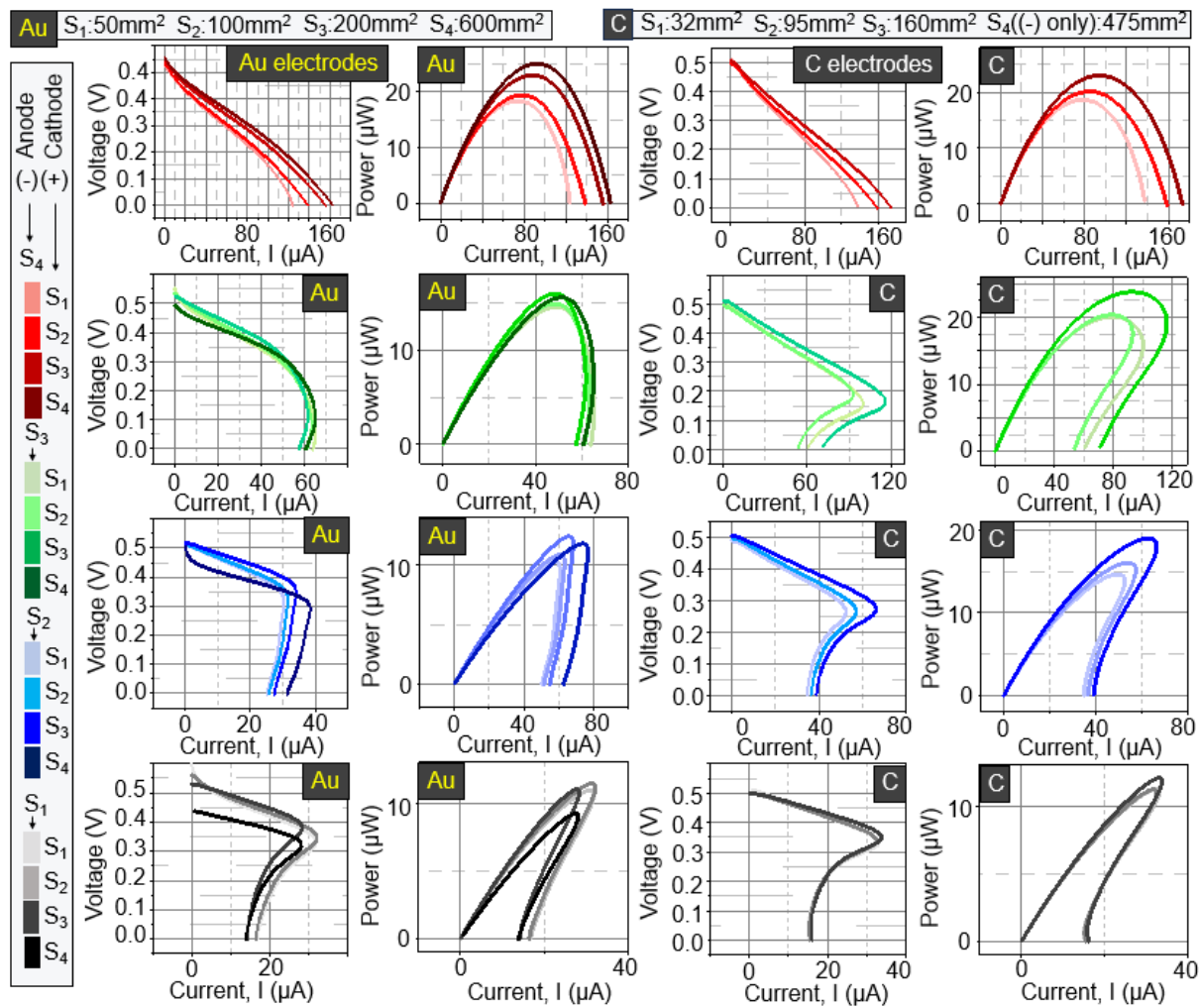


Fig. S10 Electrode material and surface area optimization. Polarization and corresponding power density curves for gold (Au) and graphite (C) electrodes of increasing surface area (S1–S4). The data demonstrate that enlarging the anode surface area markedly improves current and power output, with Au electrodes consistently outperforming graphite. Cathode enlargement provided minimal performance gains. These results directly informed the selection of Au and the prioritization of anode area in the coaxial μ MFC design.

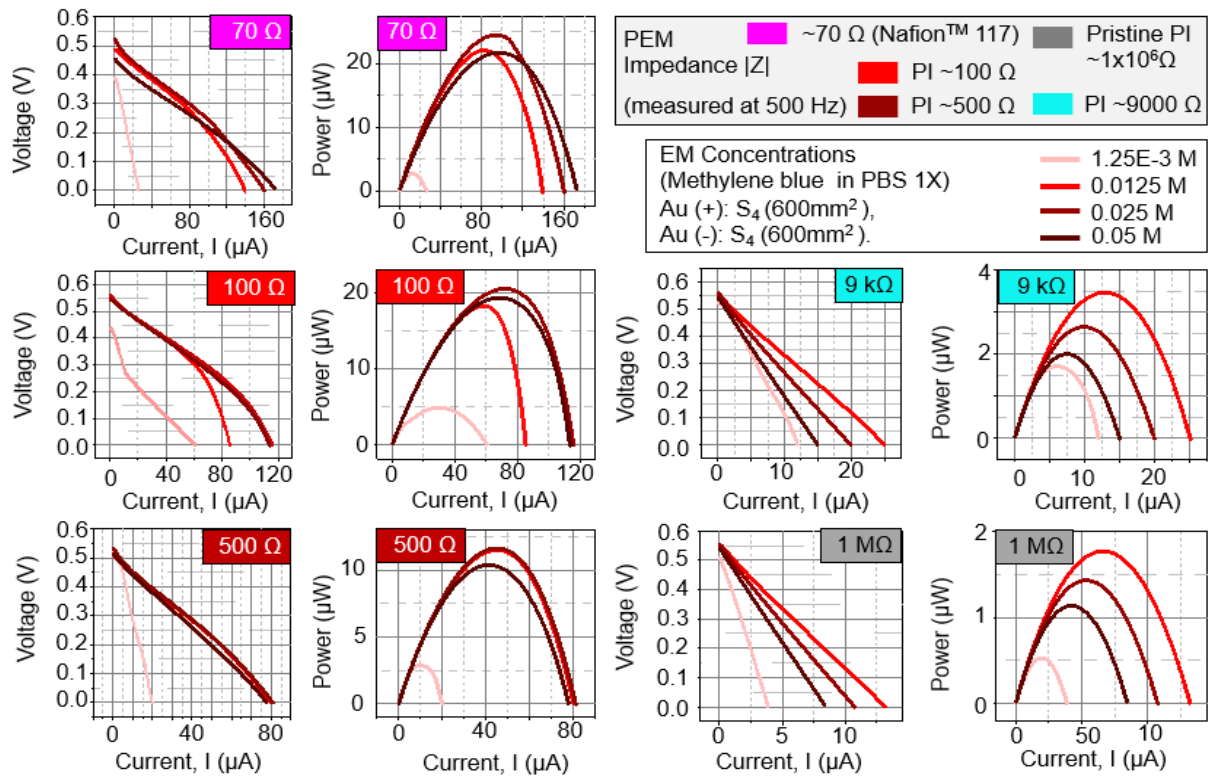


Fig. S11 Independent optimization of PEM resistance and mediator concentration. Polarization and power density curves for PI proton-exchange membranes (PEMs) of varying resistance ($70\ \Omega$ to $1\ M\Omega$) across a range of methylene blue concentrations. Low-resistance PEMs (~ 70 – $100\ \Omega$) enable high power output, while performance is progressively limited by high membrane resistance. Critically, the optimal mediator concentration window (~ 0.0125 – $0.025\ M$) is maintained across all resistances, demonstrating that proton transport and mediator kinetics constitute independent, non-competing optimization pathways.

Supplementary Video V1–5

Video V1: Independent and stable fluidic operation of inner and outer channels.

The video demonstrates the integrity of the integrated microfluidic platform, showing independent injection of orange (inner channel) and green (outer channel) fluid streams. Flow is pulsed in forward and reverse directions, confirming complete isolation between the two coaxial compartments with no observable mixing, as illustrated in the connection scheme in Fig. 3b. (Playback speed: 2x real-time)

Video V2: Controlled fluidic transfer between inner and outer channels.

This video illustrates the designed fluidic routing capability. A red dye introduced into the inner tube transfers to the outer tube via an external interconnection, subsequently flowing in the opposite direction within the outer coaxial channel. This demonstrates programmable fluidic control within the sealed microsystem. (Playback speed: 2x real-time)

Video V3: Independent filling of inner and outer channels in an open configuration.

Deionized water is shown independently filling the inner and outer tubes of the Swiss-roll structure, confirming the successful self-assembly of two distinct, continuous microfluidic channels. (Playback speed: 2x real-time)

Video V4: Sequential and controlled filling of the interwinding channels.

In an open configuration, deionized water fills the interstitial channels between the windings in a sequential manner, as guided by the SU-8 spacer design (related to Supplementary Fig. S5b). This demonstrates controlled fluidic access to the entire 3D geometry and the potential for localized fluidic addressing. (Playback speed: 2x real-time)

Video V5: Visualization of sequential interwinding filling with colored fluid.

A colored dye visually enhances the demonstration of the sequential filling process, clearly showing the controlled progression of fluid through the interwinding channels one by one, confirming efficient fluidic access to the coiled architecture. (Playback speed: 2x real-time)